The Astrophysical Journal, 766:68 (20pp), 2013 April 1 doi:10.1088/0004-637X/766/2/68

G048.66−0.29: PHYSICAL STATE OF AN ISOLATED SITE OF MASSIVE STAR FORMATION*

J. Pitann[1], H. Linz[1], S. Ragan[1], A. M. Stutz[1], H. Beuther[1], Th. Henning[1], O. Krause[1], R. Launhardt[1], A. Schmiedeke[2], F. Schuller[3], J. Tackenberg[1], and T. Vasyunina[4]
[1] Max-Planck-Institut für Astronomie (MPIA), Königstuhl 17, D-69117 Heidelberg, Germany; pitann@mpia.de
[2] Physikalisches Institut, Universität zu Köln, Zülpicher Str. 77, D-50937 Köln, Germany
[3] Max-Planck-Institut für Radioastronomie (MPIfR), Auf dem Hügel 69, D-53121 Bonn, Germany
[4] Department of Chemistry, University of Virginia, Charlottesville, VA 22904, USA
Received 2012 September 19; accepted 2013 January 2; published 2013 March 8

ABSTRACT

We present continuum observations of the infrared dark cloud (IRDC) G48.66−0.22 (G48) obtained with *Herschel*, *Spitzer*, and APEX, in addition to several molecular line observations. The *Herschel* maps are used to derive temperature and column density maps of G48 using a model based on a modified blackbody. We find that G48 has a relatively simple structure and is relatively isolated; thus, this IRDC provides an excellent target to study the collapse and fragmentation of a filamentary structure in the absence of complicating factors such as strong external feedback. The derived temperature structure of G48 is clearly non-isothermal from cloud to core scale. The column density peaks are spatially coincident with the lowest temperatures (∼17.5 K) in G48. A total cloud mass of ∼390 $M_\odot$ is derived from the column density maps. By comparing the luminosity-to-mass ratio of 13 point sources detected in the *Herschel*/PACS bands to evolutionary models, we find that two cores are likely to evolve into high-mass stars ($M_\star \geqslant 8\,M_\odot$). The derived mean projected separation of point sources is smaller than in other IRDCs but in good agreement with theoretical predications for cylindrical collapse. We detect several molecular species such as CO, HCO^+, HCN, HNC, and N_2H^+. CO is depleted by a factor of ∼3.5 compared to the expected interstellar abundance, from which we conclude that CO freezes out in the central region. Furthermore, the molecular clumps, associated with the submillimeter peaks in G48, appear to be gravitationally unbound or just pressure confined. The analysis of critical line masses in G48 shows that the entire filament is collapsing, overcoming any internal support.

Key words: ISM: clouds – ISM: individual objects (G048.66−0.29) – ISM: molecules – stars: formation – stars: kinematics and dynamics – stars: massive

Online-only material: color figures

1. INTRODUCTION

Our knowledge of the physical conditions during the very early phases of high-mass star formation ($\gtrsim 8\,M_\odot$) has been relatively limited in the past (e.g., Beuther et al. 2007), due to significant observational challenges. Consequently, the qualitative and quantitative differences in star-formation processes over different mass regimes are still strongly debated (cf. Zinnecker & Yorke 2007). In the endeavor to enhance our understanding of star formation beyond the well-studied low-mass stellar nurseries, infrared dark clouds (IRDCs) have become more and more important targets. Initially IRDCs were discovered by the *Infrared Space Observatory* (*ISO*; Perault et al. 1996) and the *Midcourse Space Experiment* (*MSX*; Egan et al. 1998). They appear as filamentary opaque structures against the diffuse galactic mid-infrared background. As IRDCs are known to be cold ($\lesssim$20 K), dense, and exhibiting high column densities ($\gtrsim 10^{23}$ cm^{-2}), they are suitable environments to form young stellar objects that can evolve into stars of intermediate to high mass (e.g., Carey et al. 2000; Rathborne et al. 2006; Ragan et al. 2006, 2009; Vasyunina et al. 2009). IRDCs were widely discussed in the context of massive star formation, but a certain fraction of IRDCs only host sub-solar to intermediate-mass star formation (Beuther et al. 2007; Kauffmann & Pillai 2010; Peretto & Fuller 2010). Still, Rathborne et al. (2006) argue that most stars in our Galaxy could form in IRDC-like molecular structures.

Most of the current theories about the formation of IRDCs treat the collapsing gaseous medium as isothermal. With the *Herschel*[5] observatory, we have the spatial resolving power, spectral coverage, sensitivity, and dynamic range to study the temperature and column density structure of IRDCs in more detail. Already one of the early *Herschel* studies using spatially resolved spectral energy distribution (SED) fitting toward an IRDC indicated a non-isothermal temperature structure (Peretto et al. 2010).

Wilcock et al. (2012) compared *Herschel* observations of IRDCs without embedded IR sources to radiative transfer models of strictly externally heated structures. They find resulting temperature profiles that go down to 11.5 K (sample average) in the center. Two further studies analyzed the temperature structure using SED fitting and a modified blackbody model. Battersby et al. (2011) present large-scale temperature maps of IRDCs. Beuther et al. (2011) studied the IRDC18454 near the W43 mini-starburst and present dust temperature maps. Both studies found temperatures higher by more than 5 K compared to the IRDCs from Wilcock et al. (2012). Further investigations have to clarify if the majority of IRDCs show similar minimum temperatures or if clumps with higher central temperatures exist. This classification is essential for the understanding of the formation process of massive stars. The comparison between dust and gas temperatures can shed light on the efficiency of the gas-dust coupling at densities typical for IRDCs. Furthermore, a

* Based on observations carried out with the IRAM 30 m Telescope. IRAM is supported by INSU/CNRS (France), MPG (Germany), and IGN (Spain).

[5] *Herschel* is an ESA space observatory with science instruments provided by European-led Principal Investigator consortia and with important participation from NASA.

well-constrained dust temperature structure can provide critical input for chemical models of IRDCs, and in particular for the dust grain surface reactions.

The goal of this paper is to accurately characterize the physical conditions of (high-mass) star formation in a relatively isolated IRDC, G048.66−0.29 (henceforth called "G48"). This case study is based on observations taken as part of the Earliest Phases of Star Formation (EPoS) Herschel guaranteed time key program (Launhardt et al. 2012; Ragan et al. 2012). We present sub-parsec scale dust temperature and column density maps and place these properties in context with the kinematic environment, probed by various molecular gas tracers (CO, HCO^+, N_2H^+, HCN, HNC). *Herschel* also enables us to characterize the embedded protostellar core population and, through the use of evolutionary models, try to understand the likely outcome of star formation in this cloud.

The kinematic distance to G48 was determined to be ∼2.7 kpc (Ormel et al. 2005), 2.5 kpc (Shipman et al. 2003; Simon et al. 2006b), or 2.6 kpc (this work). G48 appears to be projected near the giant molecular cloud (GMC) W51 (Figure 1, left), which is in fact twice as distant as G48 (Sato et al. 2010; see also Section 3.2). G48 appears isolated; therefore, we can assume that it is not strongly influenced by local heating sources. Furthermore, G48 has a quite simple mono-filamentary structure. By comparing the observational results from this isolated IRDC to more complex IRDCs (cf. Ragan et al. 2012), we can constrain the dominant effects at work for star formation in IRDCs.

Simon et al. (2006b) estimated from ^{13}CO observations an average density for H_2 associated with G48 of $\sim 3 \times 10^3$ cm^{-3}, a peak column density of 8.8×10^{21} cm^{-2}, and an LTE mass of $\sim 580\,M_\odot$. Ormel et al. (2005) identified three different clumps with masses from 91 to $130\,M_\odot$ using SCUBA and *MSX* observations. By modeling the internal velocity structure of these clumps using HCO^+ (3–2) and (4–3) single-dish data, they found that the line widths decrease outside the cloud, indicating a decrease in turbulent motions outward of the clumps. This suggests that the star formation activity inside these clumps down to the core scale is driven by turbulence.

van der Wiel & Shipman (2008) identified 13 YSOs in the vicinity of G48, based on *Spitzer* mid-infrared maps. The majority of these objects belong to "Stage I," referring to the classification scheme of Robitaille et al. (2006), and have low to intermediate masses. From a comparison of [CI] and ^{13}CO data, Ossenkopf et al. (2011) inferred the presence of a young photodissociation region (PDR) ionized by the YSOs inside of G48.

Throughout the literature the limits of sizes and masses for clumps and cores vary. In this work the spatial definition from Bergin & Tafalla (2007) is applied: cores range from 0.03 to 0.2 pc, while clumps extend over 0.3–3 pc.

Given the isolated nature and simple structure of G48, we use this source to study the collapse and fragmentation of a filamentary IRDC. Through the characterization of the point sources the evolutionary stage can be assessed a final stellar mass can be estimated from different models. Furthermore, the *Herschel* maps are utilized to study the temperature and column density structure of G48. Molecular line observations provide information about the morphology of the clumps and clues to the pressure support therein. We assess the level of freeze-out by studying the CO depletion in the central part of the IRDC.

The next section describes the observations, the data reduction, and some basic data processing steps for *Herschel*, *Spitzer*, submillimeter continuum, and molecular line observations. Section 3 details the scientific analysis and the direct results. In Section 3.1 the structure and environment of G48 are described. The measured distances for G48 and other sources in the near projected distance are discussed in Section 3.1. The temperature mapping, utilizing *Herschel*, SCUBA, and ATLASGAL data, is delineated in Section 3.3. Section 3.4 compares the column densities with other observations and estimates mass for the whole IRDC. Section 3.5 addresses the fitting and classification of point sources from the MIPS 24 μm and PACS bands. Section 3.6 contains the analysis of the molecular line data. Section 4 discusses the results in respect to previous studies of IRDC and theoretical considerations. Section 5 summarizes the main results.

2. OBSERVATIONS, DATA REDUCTION, AND PROCESSING

2.1. Herschel

In this paper we present results from the *Herschel* GTO key program—EPoS. The high-mass portion of EPoS is compiled from different surveys. The sample includes a sub-sample of "classical" IRDCs, a selection of IRDCs in the near vicinity of high-mass protostellar objects (HMPOs), and cold, massive, compact sources detected by the ISO Serendipity Survey (ISOSS). For a detailed discussion of this sample and the underlining selection strategy we refer the reader to the overview paper by Ragan et al. (2012).

The EPoS observations were supplemented with data from the "Herschel infrared Galactic Plane Survey" (Hi-GAL) project, done with the Photometer Array Camera and Spectrometer (PACS; Poglitsch et al. 2010) and the Spectral and Photometric Imaging Receiver (SPIRE; Griffin et al. 2010) on board the *Herschel Space Observatory* (Pilbratt et al. 2010).

2.1.1. PACS

The EPoS PACS scan maps at 70 μm, 100 μm, and 160 μm were obtained with the medium scan speed of 20″ s^{-1} and the nominal scan leg length of 7′. The data were processed to level-1, i.e., calibrated and converted to physical units, using HIPE (Ott 2010). We applied a second-level deglitching to flag bad data values by σ-clipping flux values mapped on to each pixel. The "time ordered" option was used, and a 25σ threshold was applied. The level-2 products, i.e., fully reduced fits maps, were obtained using SCANAMORPHOS (Roussel 2012) version 5.0 instead of applying the nominal HIPE high-pass filtering and photProject reduction step, due to the improved performance of SCANAMORPHOS (see Ragan et al. 2012). The maps in each band were reduced with a pixel size of 1.″0 pixel^{-1}.

2.1.2. SPIRE

The EPoS SPIRE scan maps at 250 μm, 350 μm, and 500 μm were obtained with a scan speed of 30″ s^{-1}. They were reduced up to level-1 using HIPE version 5.0 with the calibration pool 5.1. The final level-2 reduction was done with SCANAMORPHOS version 9.0 using the "galactic" option. The pixel sizes are 6.″0 pixel^{-1} at 250 μm, 10.″0 pixel^{-1} at 350 μm, and 14.″0 pixel^{-1} at 500 μm.

2.1.3. Hi-GAL

To include a larger coverage, we obtained the raw data products from the Hi-GAL Open Time Key Project. These observations were carried out in the PACS/SPIRE parallel

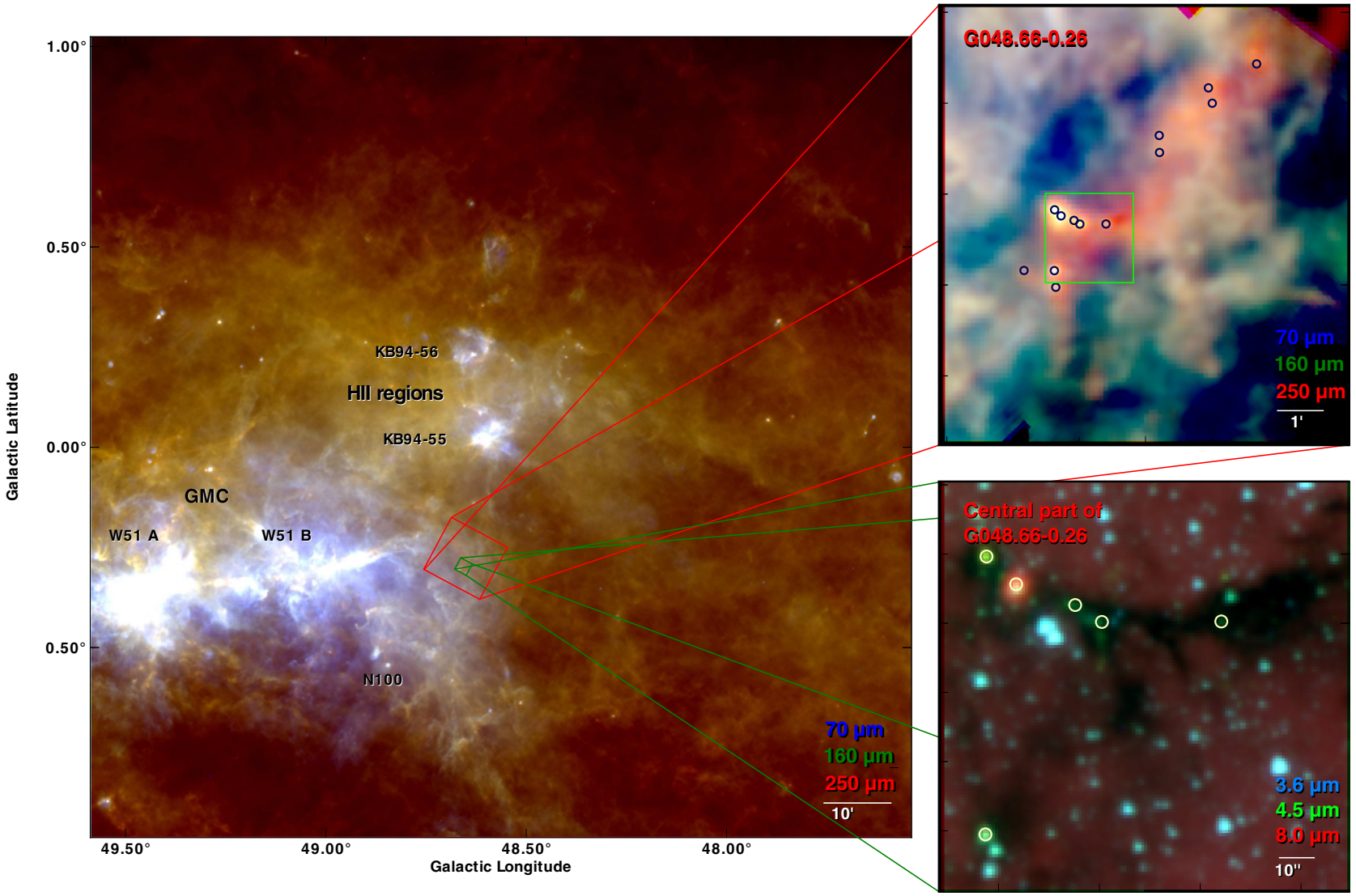

Figure 1. Left panel presents a *Herschel* map of the galactic neighborhood of G48. The dominant feature to the left of G48 is the giant molecular cloud complex of W51. Two H II regions described by Kuchar & Bania (1994) are located above G48. Below G48 the infrared bubble N100 appears. The map is composed of the PACS band at 70 μm (blue), 160 μm (green), and SPIRE at 250 μm (red) from the Hi-GAL field 48_0. The top right panel is a zoom into the whole IRDC. It uses the same *Herschel* bands, utilizing the EPoS observations. The bottom right panel shows the central part of G48 as an IRAC three-color image (3.5, 4.8, 8.0 μm). The green band shows elongated lobes attributed to shock-excited H_2, sometimes referreed to as "green and fuzzy" features "or extended green objects" (EGOs). The detected *Herschel* point sources from Section 3.5 are indicated by circles in the right panels. All intensities are plotted with logarithmic scaling in all maps.

(A color version of this figure is available in the online journal.)

mode with a scan speed of 60″ s^{-1}, resulting in large-scale maps. The 70 μm and 160 μm PACS maps have been reduced using HIPE 8.0, applying the same options as for the EPoS PACS data. Level-2 processing has been performed with SCANAMORPHOS version 15. The pixel size is 3.″2 pixel^{-1} for both maps. The 250 μm, 350 μm, and 500 μm SPIRE maps were reduced up to level-1 using HIPE version 8.0 with the calibration tree 8.1. SCANAMORPHOS version 15 was used to produce the level-2 maps. The pixel size is the same as for the EPoS SPIRE maps. The final maps are presented in the left panel of Figure 1. The Hi-GAL maps are used for the temperature mapping in Section 3.3.

2.1.4. Photometry, Point-source Detection

Due to the diffuse and heterogeneous background emission varying on a wide range of spatial scales, it is more robust to perform point-spread function (PSF) photometry than aperture photometry. Therefore, the `starfinder` PSF photometry software (Diolaiti et al. 2000) was used for the point-source detection and flux extraction for the PACS bands. The latest empirical PSF of the Vesta asteroid was used (OD 160), obtained from the Herschel Science Archive (HSA), since an empirical PSF derived from sources in G48 is noise dominated and therefore less acceptable. For consistency the PSF maps were reprocessed with SCANMORPHOS and rotated to the orientation of the maps. The noise in the PACS maps is not white noise, since it suffers from pixel-to-pixel correlations induced, e.g., by non-thermal low-frequency noise. To calculate the average noise in the map, a Gaussian-distributed noise was assumed, but corrected by a factor for the pixel-to-pixel correlation.

The major source of confusion in the source detection is the complicated background. In particular, the bright background toward the GMC returns numerous false detections. We only include regions of the PACS maps that correspond to regions in the ATLASGAL map (see Section 2.3) with fluxes above a 3σ level. To further improve the detection efficiency, an unsharp mask filter was applied in each PACS band by subtracting a median-smoothed map from the respective science frame. With this procedure we avoid false detections and miss three obvious sources for the automated detection run. These sources were then included in the catalog identified by eye as clear detections. With the compiled fixed source positions the final photometry was performed on the non-filtered science frames. To be considered a detection, a source must meet the following conditions: it must have a source flux above the 5σ noise level and be detected in all PACS bands within the FWHM of the 160 μm PACS PSF (∼11.″2). The results of the point-source extraction are reported in Section 3.5. The given fluxes are already color-corrected for the source temperatures.[6] Further details of the source extraction are given in the EPoS high-mass overview paper (Ragan et al. 2012).

2.2. Spitzer

We obtained the *Spitzer* IRAC and MIPS maps from the Galactic Legacy Infrared Mid-Plane Survey Extraordinaire (GLIMPSE; Benjamin et al. 2003) and the MIPS Inner Galactic Plane Survey (MIPSGAL; Carey et al. 2009). The 24 μm MIPSGAL maps were processed with the MIPS Data Analysis Tool (DAT v3.10; Gordon et al. 2005) starting from the `raw` data products.

We used the 8 μm IRAC map to create an extinction map. PSF photometry was performed on this map, using the `starfinder` package. An averaged, empirical PSF was used to remove all the point sources in this field. The residual map was used to compute the optical depths. One of the key problems in calculating an optical depth in IR data is to determine the foreground and background intensities. Several different methods are described in the literature (e.g., Simon et al. 2006a; Butler & Tan 2009; Ragan et al. 2009; Butler & Tan 2012). However, to estimate the optical depth in one single cloud, we used the method described in Vasyunina et al. (2009):

$$\tau = \ln\left(\frac{I_0 - I_{\rm fg}}{I_{\rm IRDC} - I_{\rm fg}}\right), \quad (1)$$

where $I_{\rm IRDC}$ is the flux derived from the IRDC directly and I_0 is measured "off-cloud" in a nearby region meant to represent the characteristic unattenuated MIR emission. I_0 (and $I_{\rm IRDC}$) contains contributions from both the foreground and background (i.e., $I_0 = I_{\rm bg} + I_{\rm fg}$), and only $I_{\rm bg}$ is needed to computed the optical depth. For $I_{\rm fg}$, we assume the zodiacal light emission provided in the header of the IRAC data product. This is a lower limit to the true foreground. Nevertheless, the uncertainties in the column densities are dominated by what is assumed about the extinction law (factor 2 to 3), whereas the $I_{\rm fg}$ contributes about an error less than 50%.

The point-source fluxes from MIPS 24 μm used in Section 3.5 were also obtained with `starfinder`. For MIPS PSF photometry we utilized a model PSF computed by the `STINYTIM`[7] program, based on `TINYTIM` for the *HST* (Krist 2002).

The spectrum, shown in Figure 2, was obtained from the Infrared Spectrograph (IRS) on board the *Spitzer Space Telescope*. The observation (AOT: 12093696) was taken from the Spitzer Heritage Archive (SHA) as part of the "Infrared Dark Clouds in the Inner Galaxy" program. We used a pipeline partly based on the SMART package and the FEPS spectral extraction tools (Bouwman et al. 2006; Swain et al. 2008; Pitann et al. 2011). The background-subtracted on-source spectrum and the background spectra from the off-source nod-positions are shown in Figure 2. Only the long-wavelength order (LL) is reduced, since the slit for the short wavelength did not cover any point source in the IRDC. The LL slit did only cover about 60% of the SMART-source PSF, which leads to a flux leakage in the continuum flux. But line shapes and line fluxes should be unchanged for the source spectrum, except for a lower signal-to-noise ratio. A strong [S III] emission appears over the whole IRS slit, leading to an artifact in the source spectrum due to an oversubtraction of the background. The source spectrum was corrected for this artifact using a polynomial background fit (see Section 3.2.3 in Pitann et al. 2011).

2.3. Submillimeter Imaging

We utilized submillimeter data from the SCUBA Legacy Catalogue (Di Francesco et al. 2008). The 450 and 850 μm observations were part of the fundamental catalog with an effective beam size of 17.″3 and 22.″9, respectively. Given the better sensitivity of the survey, the 870 μm observations from the "APEX Telescope Large Area Survey of the Galaxy" (ATLASGAL; Schuller et al. 2009) were used in the temperature fitting (Section 3.3) and to determine column densities (Section 3.4).

[6] See: http://herschel.esac.esa.int/twiki/pub/Public/PacsCalibrationWeb/cc_report_v1.pdf

[7] See: http://irsa.ipac.caltech.edu/data/SPITZER/docs/dataanalysistools/tools/contributed/general/stinytim/

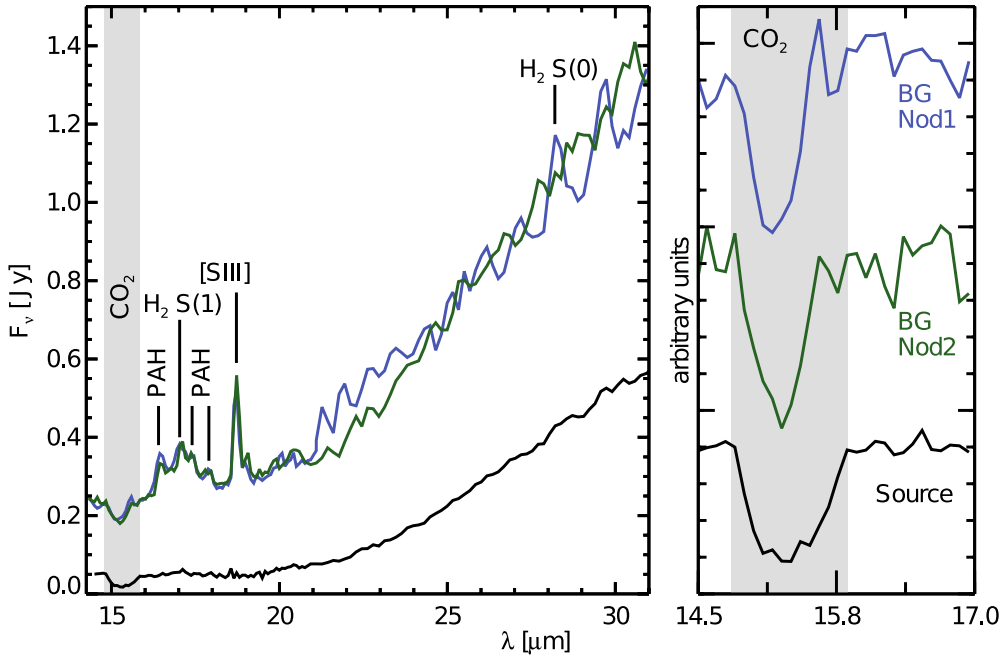

Figure 2. LL-spectrum from Source 2 from IRS/*Spitzer* is shown. In the left panel the source spectrum is plotted in black and the extracted background spectra are shown in blue and green. The background spectrum extracted in the first nod position (BG Nod 1) pointed toward the GMC, while the second background spectrum is taken at the western edge of the IRDC (BG Nod 1). The atomic [S III] line is present as a bright extended emission over the whole slit. The CO_2 ice absorption band is underlined in light gray. The right plot shows the baseline-subtracted CO_2 profiles.

(A color version of this figure is available in the online journal.)

The corresponding beam size for the ATLASGAL data is around 19.″2. The rms noise level for ATLASGAL is ∼50 mJy.

2.4. Millimeter Line Observations

We obtained molecular line data using the 22 meter MOPRA radio telescope and the MOPRA spectrometer (MOPS), operated by the Australian National Facility (ATNF). The observations were performed with the 3 mm band receiver (90 GHz) in the "On-the-fly Mapping" mode (OTF) with a beam size of 36″ at 86 GHz and 33″ at 115 GHz. Using MOPS in the "Zoom" setup allowed us to observe 13 lines simultaneously (^{13}CS, C_2H, CH_3CCH, CH_3CN, $H^{13}CN$, HCO^+, $H^{13}CO^+$, HCCCN, HCN, HNC, HNCO, N_2H^+, SiO).

Most of these lines are good tracers for dense gas (see Vasyunina et al. 2011 for a detailed description of each molecular species). However, the rms noise for all MOPRA maps is only slightly below 0.1 K, which allows us to detect line emission above 3σ only in the HCN, HNC, HCO^+, and N_2H^+ maps.

The spectrometer configuration results in a velocity resolution of ∼0.11 km s^{-1}. The main-beam efficiency varies between 49% at 86 GHz and 44% at 100 GHz (Ladd et al. 2005). The typical system temperatures were between 210 and 290 K. The ^{13}CO (1–0) data products were obtained from the Galactic Ring Survey (GRS; Jackson et al. 2006) performed by the Five College Radio Astronomy Observatory (FCRAO). With an angular resolution of 46″ the beam of FCRAO is somewhat larger than that of MOPRA. The rms noise level in the GRS map is below 0.9 K.

We obtained ^{13}CO (2–1) and C^{18}O (2–1) maps using the 230 GHz heterodyne receiver array (HERA; Schuster et al. 2004) at the IRAM 30 m telescope. The average FWHM of the HERA beam is 11.″3, which is much better compared to MOPRA or FCRAO. The rms noise level is below 0.5 and 0.3 K in the ^{13}CO and C^{18}O HERA maps, respectively.

To acquire methylacetylene ($CH_3C \equiv CH$), data observations were performed with the IRAM 30 m telescope in position switching mode. For these observations the EMIR receiver with Fast Fourier Transform Spectrometer (FTS) as a back end was used. Total time On source and Off source was 33 minutes. The Off source position was chosen 600″ away from the On source position. The On source position was pointed at $19^h21^m49.^s9$, +13°49′34.″7 (FK5, J2000). The pointing was checked every hour, giving a pointing accuracy better than 3″. The typical system temperature during observations was about 200 K. At 153 GHz the telescope beam size is 16″ and the beam efficiency is 0.73. The data were analyzed using GILDAS/CLASS software.

A list of physical parameters for each observed line is given in Table 1.

3. RESULTS

3.1. Morphology—From Large to Small Scales

The left panel of Figure 1 shows the galactic neighborhood of G48. The image is composed of the 70, 160, and 250 μm Hi-GAL maps in blue, green, and red, respectively. A global brightness gradient toward the outer parts of the galactic plane is present over the whole image. In the vicinity of G48 the GMC W51 is observed. The cloud complex W51A and W51B have an angular distance of ∼15′ and ∼50′ to G48, respectively. The EPoS maps (Figure 1, top right panel), in particular the PACS observations, show a brightness gradient toward W51 and the infrared bubble N100 (Churchwell et al. 2006). W51 and G48 are not physically connected since recent observations place W51 twice as far away as G48 (see next section).

In the *Spitzer* IRAC 8 μm and the MIPS 24 μm channels the IRDC appears as the typical dark filamentary absorption feature against the diffuse galactic emission background (see

Table 1
Molecular Lines

Molecule	Trans.	ν_r (GHz)	$\Delta V_{\rm therm}$ (km s^{-1})	A_{ul} (10^{-5} s^{-1})	E_u/k_B (K)	$n_{\rm crit}$ (cm^{-3})	Beam Size (arcsec)	Instrument	Obs. Date
HCO^+	1–0	89.188523	0.166	3.0	4.28	2.1×10^5	38″	MOPRA	2010 Jul 7–9
HCN	1–0	88.631602	0.172	2.4	4.25	1.5×10^6	38″	MOPRA	2010 Jul 7–9
HNC	1–0	90.663568	0.172	2.690	4.35	3.2×10^5	38″	MOPRA	2010 Jul 7–9
N_2H^+	1–0	93.173700	0.166	3.6	4.47	1.8×10^5	38″	MOPRA	2010 Jul 7–9
^{13}CO	1–0	110.201354	0.166	0.0063	5.29	1.9×10^3	44″	FCRAO	Archive data[a]
^{13}CO	2–1	220.398684	0.166	0.0604	15.87	2.0×10^4	11.″25	IRAM/HERA	2012 Jan 23
$C^{18}O$	2–1	219.560319	0.163	0.0601	15.81	1.9×10^4	11.″25	IRAM/HERA	2012 Jan 23
CH_3C_2H	9_0–8_0	153.8172	0.142	8.75			16″	IRAM/EMIR-FTS	2011 Jun 10/12
CH_3C_2H	9_1–8_1	153.8142	0.142	8.44			16″	IRAM/EMIR-FTS	2011 Jun 10/12
CH_3C_2H	9_2–8_2	153.8054	0.142	7.55			16″	IRAM/EMIR-FTS	2011 Jun 10/12
CH_3C_2H	9_3–8_3	153.7907	0.142	12.52			16″	IRAM/EMIR-FTS	2011 Jun 10/12
CH_3C_2H	5_1–4_1	85.455665	0.142	0.1948	19.53		38″	MOPRA	2010 Jul 7–9
$H^{13}CN$	1–0	86.339860	0.169	2.2256	4.14	2.6×10^6	38″	MOPRA	2010 Jul 7–9
$H^{13}CO^+$	1–0	86.754288	0.164	3.8534	4.16	1.9×10^5	38″	MOPRA	2010 Jul 7–9
SiO	2–1	86.846960	0.135	2.927	6.25	1.9×10^6	38″	MOPRA	2010 Jul 7–9
C_2H	2–1	87.316925	0.179	0.1528	4.19	2×10^5[b,c]	38″	MOPRA	2010 Jul 7–9
HNCO	$4_{0,4}$–$3_{0,3}$	87.925238	0.137	0.9024	10.55	4.5×10^6	38″	MOPRA	2010 Jul 7–9
HC_3N	10–9	90.978865	0.125	5.812	24.01	7.5×10^4	38″	MOPRA	2010 Jul 7–9
CH_3CN	5_1–4_1	91.985316	0.140	6.0800	20.39	4×10^5[c]	38″	MOPRA	2010 Jul 7–9
^{13}CS	2–1	92.494308	0.134	1.4124	6.66	5.0×10^5	38″	MOPRA	2010 Jul 7–9

Notes. The columns list the molecular species, the transition, the rest frame frequency, the thermal line width at 17.3 K, the Einstein coefficient, the upperstate energy, the critical densities and the angular resolution for our observations, the used instrument, from left to right, respectively. The upper part of the table presents the detected molecular lines, while the bottom part lists the MOPRA lines lacking a 3σ detection.
[a] From the Galactic Ring Survey with FCRAO.
[b] From Lo et al. (2009).
[c] From Sanhueza et al. (2012).

Figure 3). G48 is extended over ∼7.′5 in the north-south direction. The dark cloud can be roughly divided into three parts. The central region of the IRDC appears as a elongated structure of ∼2.′3 in east-west orientation. This region has the brightest submillimeter emission. The western part of the central region shows the highest extinction in the *Spitzer* maps. Only this part of the IRDC appears in clear absorption in all three PACS channels. Furthermore, this part is clearly associated with the most massive submillimeter clump, called "extinction peak" (EP, with a mass of ∼130 $M_\odot$ from SCUBA observation) in Ormel et al. (2005). The eastern part of the central IRDC only shows clear extinction in the *Spitzer* bands. In the *Herschel* PACS maps this region is dominated by compact background emission from embedded point sources, in particular Source 1 (see Section 3.5). The central region, as the rest of G48, appears as a diffuse emission structure in the SPIRE maps, but two compact sources can be identified in the eastern central part. The peak positions of these emission features detected at 250 μm and 350 μm are in good agreement with the peak positions of two submillimeter clumps (P1 with 91 $M_\odot$ and P2 with 100 $M_\odot$) identified by Ormel et al. (2005). Due to the lower resolution of the 500 μm SPIRE channel, the two positions are not resolved.

The structures found south- and northward of the central part of the IRDC appear more diffuse in the *Spitzer* bands and are barely recognizable in the PACS channels. In contrast, in the SPIRE bands these diffuse absorption features appear as an elongated emission structure. While this emission is diffuse in the northern part, compact emission is detected in good agreement with the SCUBA and ATLASGAL data in the southern part of the IRDC. The associated submillimeter peak was called "P3" in van der Wiel & Shipman (2008; see Figure 3).

3.2. Distance

The LSR velocities found for the different clumps and molecular species do not differ by more than 3 σ_V. This results in a weighted mean velocity of $\langle V_{\rm LSR}\rangle = 33.91 \pm 0.05$ km s^{-1} (see Section 3.6). The resulting kinematic distance for G48 is 2.6 ± 0.6 kpc. This value is used for all calculations in this paper. We derive kinematic distances using the Reid et al. (2009) algorithm, which takes into account trigonometric parallax measurements of masers in high-mass star-forming regions in the Galaxy, applied to a disk Galaxy model. We use their standard derived rotational parameters of $\Theta_0 = 254$ km s^{-1} and $R_0 = 8.4$ kpc.

The Hi-GAL three-color image (Figure 1) shows G48 at a close projected distance to the GMC W51 and several objects, as, e.g., H II regions, infrared bubbles, and other bright point sources. Water maser observation estimates a distance of ∼5.4 kpc for W51 (Sato et al. 2010). Known distances of infrared bubbles (S. Kendrew 2012, private communication) and sources from the rms survey catalog (e.g., massive YSO, H II regions; Urquhart et al. 2008) in the vicinity of G48 have a distance of more than 5 kpc. Moreover, no CO is detected in the global GRS maps outside of G48 at its typical LSR velocities.

We therefore conclude that G48 is an isolated region, making it a unique IRDC.

3.3. Herschel Temperature Map

To create temperature and column density maps of G48, we used *Herschel* maps and ground-based submillimeter data. In brief, the basic steps we have taken to fit the temperature and column density maps are as follows:

1. The global background flux offsets are estimated from the large-scale Hi-GAL maps and subtracted from the maps.

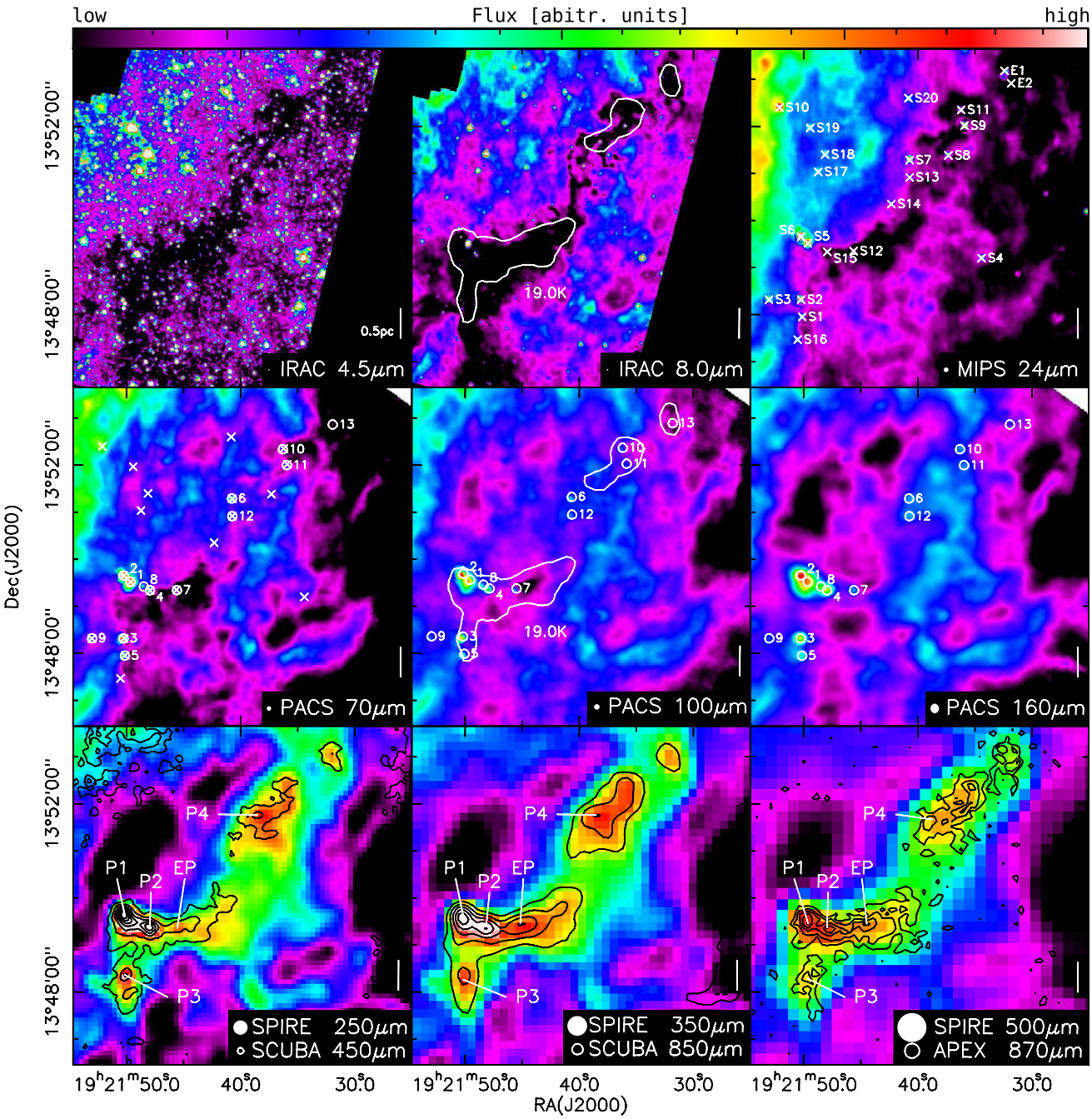

Figure 3. Intensity plots for G48 are shown in the different *Spitzer*, PACS, and SPIRE channels. Each plot is shown on a linear scale to highlight absorption or emission at each wavelength band; the top color bar indicates the relative flux scale. The positions of the 24 μm point sources as characterized by van der Wiel & Shipman (2008) are indicated by red crosses in the MIPS 24 μm and PACS 70 μm maps. The MIPS 24 μm sources from van der Wiel & Shipman (2008) are labeled "S," while two additional 24 μm sources associated with G48 are labeled "E1" and "E2." The detected sources in the PACS bands are marked by the white circles. The radius of the circles implies the fitting radius between the different bands. The SPIRE maps are overlaid by SCUBA 450 μm, 850 μm, and ATLASGAL 850 μm contours, respectively. The corresponding beam sizes for *Spitzer*, PACS, and SPIRE are indicated with circles in each panel. An isothermal contour of 19 K from the temperature fitting (Section 3.3) is overplotted for IRAC 8 μm and PACS 100 μm. The beam size of the observations plotted in contours is plotted as open ellipses. The white bar (right side) gives a projected scale of 0.5 pc on the map.

(A color version of this figure is available in the online journal.)

2. All data (PACS at 160 μm, SPIRE at 250 and 350 μm, SCUBA at 450 μm, and ATLASGAL 870 μm) were convolved to a common limiting beam size (SPIRE 350 μm) and converted to uniform units (Jy arcsec^{-2}). The inclusion of the also available SPIRE 500 μm data would force us to commonly convolve all other maps to a coarse resolution of around 36″. We therefore neglect these 500 μm data for the temperature mapping.
3. In the final fitting process an SED was fitted to each pixel using a modified blackbody function, requiring at minimum three data points for the SED.

For the final pixel-to-pixel SED fitting a careful preparation of the initial data is needed. A complete description of the data treatment and fitting process is given in Launhardt et al. (2012). The observed globules in Launhardt et al. (2012) are more isolated, and suitable background flux offsets can be calculated

within the EPoS maps. Unfortunately, the larger extent of the IRDC, the imprint of the adjacent GMC and infrared bubble (see Section 3.1), and the limited map sizes prevent a reasonable background determination. To overcome these limitations, we utilized *Herschel* maps from the Hi-GAL program, which cover a much larger area. We extracted the background fluxes from a low-emission region off the galactic plane located at $19^{h}23^{m}26\overset{s}{.}018$, $+12^{\circ}37'28\overset{''}{.}06$ (J2000) with a box size of 500″. The actual method to extract the background fluxes in this field with relatively low spatial variations is adopted from Stutz et al. (2009). It is an iterative Gaussian fitting algorithm applied to the pixel flux distribution in the selected region. The best fit to the background levels is found by omitting the non-Gaussian components. Finally, background levels of 0.040 Jy pixel^{-1} and 1.434 and 1.191 Jy beam^{-1} were computed for 160, 250, and 350 μm, respectively.

Battersby et al. (2011) used a large-scale Gaussian profile to remove the Galactic background from their observed Hi-GAL maps toward two different fields before the SED fitting. *Herschel* temperature maps of a sub-region close to the star-forming complex W43 were created by Beuther et al. (2012) without any global background subtraction. For lower temperatures (<25 K) both methods just differ by 1–2 K. Our maps appear to be more sensitive to the background determination;[8] however, changing our estimated background level by ±50% does not have a significant impact on the derived temperatures.

For the SED fitting all *Herschel* maps (PACS 160 μm, SPIRE 250 and 350 μm) were convolved to the SPIRE 350 μm beam, using the kernels from Aniano et al. (2011). For the submillimeter maps (SCUBA 450 μm and APEX 870 μm) a Gaussian kernel was used. For this step all maps were calibrated in units of Jy arcsec^{-2}.

In the resulting maps the remaining emission per pixel is assumed to be well represented by modified blackbody emission:

$$S_{\nu}(\nu) = \Omega(1 - e^{-\tau(\nu)})B_{\nu}(\nu, T_{\rm d}), \quad (2)$$

with

$$\tau(\nu) = N_{\rm H}\, m_{\rm H}\, R\, \kappa(\nu), \quad (3)$$

where $S_{\nu}(\nu)$ is the observed flux density for a given frequency ν and solid angle Ω (all fluxes are normalized to Jy arcsec^{-2}), $\tau(\nu)$ the optical depth, $B_{\nu}(\nu, T_{\rm d})$ the Planck function, $T_{\rm d}$ the dust temperature, $m_{\rm H}$ the proton mass, R the dust-to-gas mass ratio, and $N_{\rm H} = 2 \cdot N({\rm H}_2) + N({\rm H})$ the total hydrogen column density. For the column density map (Figure 5, bottom left) we assume that all hydrogen is present as molecular gas in G48. For the dust opacity κ we adopt the model from Ossenkopf & Henning (1994) for thin ice mantels and a gas density of 10^5 cm^{-3}. For the hydrogen-to-dust mass ratio we adopted a value of $R = 110$ (e.g., Sodroski et al. 1997). To account for helium and heavy elements, one would choose a total gas-to-dust mass ratio 1.36 times higher. A modified blackbody function, as in Equation (2), was fitted individually for each pixel using $N_{\rm H}$ and $T_{\rm d}$ as free parameters with a χ^2 minimization. The Hi-GAL data include only the 70 and 160 μm maps for the PACS bands. To avoid contributions from stochastically heated small grains or optical thick emission, we exclude the 70 μm band (e.g., Battersby et al. 2011; Pavlyuchenkov et al. 2012). Usually the fluxes in the three remaining *Herschel* bands (160, 250, and 350 μm) are well constrained and provide a good fit to the modified blackbody function. Therefore, every shown pixel in the temperature map (Figure 5) results from an SED fit of at least these three Herschel bands. If one of the submillimeter (450 or 870 μm) fluxes deviates by more than 3σ from the SED fluxes constrained in the other bands, it is not used in the temperature and column density calculation.

The temperature map (Figure 5, bottom right) shows a steep drop at the boundaries of G48 within the resolution limits set by the size of the convolution kernels (a 19 K contour is overplotted on the IRAC map at 8 μm and PACS at 100 μm in Figure 3). In the central region of G48, with the strongest submillimeter emission, the temperatures drop below 18 K (white contour in Figure 5, bottom right). The local minima agree with the position of the submillimeter peaks P1 (17.1 K), P2 (16.8 K), and EP (17.1 K). In general, our observed line-of-sight temperatures are higher than the ones (10–15 K) found by Ormel et al. (2005) for P1, P2, and EP. However, the later temperature profiles from Ormel et al. (2005) are obtained from fitting observational results to core models (similar to Wilcock et al. 2012; see Section 4.5).

To assess the uncertainties of our line-of-sight-averaged temperatures, we investigated how the change of different parameters influences the resulting temperatures and column densities. When altering the subtracted global background level, which is subtracted from the Herschel maps, by ±50% before the fitting process and using different beam sizes for the convolution, the resulting temperatures are found to differ by no more than 0.3 K inside the IRDC, where dust emission is detected in the ATLASGAL maps. In the temperature fitting routine, we assume mean absolute background flux levels that were derived for regions well outside the galactic plane (see Launhardt et al. 2012) and might not be appropriate for this IRDC. For lack of better estimates of the local absolute background levels, we have tested the effect of simply amplifying those background levels by a factor of 100. The resulting temperatures and column densities in the IRDC were found to change by no more than 0.1 K and 2.5%, respectively. The effect would be stronger for lower column densities, which we do not consider here. Hence, we can robustly conclude that the effect of the uncertain knowledge in the absolute local background flux levels on the derived temperatures and column densities in the IRDC is smaller than the uncertainties introduced by the calibration, data reduction, and dust opacity models and is thus negligible.

The total relative uncertainties introduced by calibration and data reduction are found to be 2.5% for the temperatures and 10% for the column densities. The largest uncertainties are introduced by the uncertain knowledge of the underlying dust opacity model. Therefore, we assume an overall temperature uncertainty of ±1 K. A more detailed discussion of the different contributions to the uncertainties can be found in Launhardt et al. (2012).

It should be mentioned that the temperatures outside G48 are not very reliable because of the brightness gradient introduced by W51 and N100, as mentioned earlier. In the column density and temperature maps (Figure 5) the point-source positions and temperatures are indicated.

The temperatures derived at the locations of the point sources in the large-scale temperature map are discrepant from the temperatures derived by fitting the individual SEDs of said point sources, the later of which were extracted at native resolution.

[8] We also determined the background offsets from a field with low spatial variations and almost no compact emissions inside the galactic plane. But the resulting temperature maps from the SED fitting were suspiciously high (>20 K inside the IRDC). Therefore, we decided to estimate the background offsets further outside of the galactic plane.

This discrepancy is not surprising as it is caused by beam convolution in the temperature map and the inclusion of longer wavelengths.

3.4. Column Densities

To estimate the column densities for G48, we utilized three different methods: mid-infrared extinction map from IRAC at 8 μm, submillimeter dust emission, and modified blackbody fitting including *Herschel* and submillimeter data (see Section 3.3).

The IRAC 8 μm extinction maps provide us with an estimate of the optical depth per pixel (see Section 2.2). These optical depths were converted into column densities (Figure 5, bottom left) using (Vasyunina et al. 2009)

$$N_{\rm H_2} = 1.086\ \tau / C_{\rm ext}, \quad (4)$$

where τ is the optical depth per pixel and $C_{\rm ext}$ is the extinction cross section. The nature of the mid-infrared extinction law below 10 μm in IRDCs and massive star-forming regions is still a matter of debate (e.g., Butler & Tan 2009). In agreement with findings of Indebetouw et al. (2005), we used an extinction factor of $R_V = 5.5$ to parameterize the extinction cross section $C_{\rm ext}$. We choose $C_{\rm ext} = 4.62 \times 10^{-23}$ cm^2 from Weingartner & Draine (2001, (case B)). The derived column densities also depend on the assumed R_V value and, therefore, the used extinction cross section. The extinction factor $R_V = 3.1$ is more representative of the diffuse ISM and would result in significantly higher column densities. Another effect for the 8 μm extinction is the saturation of the column density for high values; therefore, the masses based on IRAC 8 μm, discussed further below, can only be lower limits (for a detailed discussion, see Vasyunina et al. 2009).

The second method to determine the hydrogen column densities utilizes the dust emission detected in the 870 μm map from ATLASGAL:

$$N_{\rm H_2} = \frac{R F_\nu}{B_\nu(\nu, T_d) m_{\rm H_2} \kappa\ \Omega}, \quad (5)$$

where F_ν is the submillimeter flux, $R = 110$ the gas-to-dust ratio, $B_\nu(\nu, T_d)$ the Planck function for a given wavelength (870 μm) and dust temperature ($T_d = 17.3$ K or 19.2 K; see below), $m_{\rm H_2}$ the mass per hydrogen molecule, and Ω the beam size. We adopt a mass absorption coefficient of $\kappa = 1.47$ cm^2 g^{-1} from Ossenkopf & Henning (1994; thin ice mantel, 10^5 cm^{-3}, as in Section 3.3).

We have three independently derived column density maps: IRAC 8 μm, ATLASGAL 870 μm, and the SED-fitted map combining *Herschel* and ATLASGAL. Each one requires us to make different and independent assumptions in order to derive column densities; furthermore, they also vary widely in angular resolution.

For example, the 8 μm extinction map, which has a resolution of $\sim 3''$, requires an assumption of a certain extinction factor for the dust extinction cross section, optically thin emission, and the local background contribution ($I_{\rm BG}$ in Equation (1)) but is temperature independent. Furthermore, the residuals of the PSF removal for bright IRAC point sources with compact background emission can result in an underestimate of local column density (see, e.g., source 1 in Figure 5, top left).

For the ATLASGAL 870 μm map, with a resolution of $\sim 19''$, always a fixed temperature is assumed, requiring optically thin emission and a dust opacity choice at the wavelength of interest.

While the SED-fitted map also requires a dust model assumption, it contains information from multiple wavelengths and simultaneously derives $N_{\rm H_2}$ and temperature for each pixel, under the assumption that the mass is well represented by a modified blackbody and assuming a fixed spectral index β. Therefore, the derived column densities can be considered more robust compared to the two previous methods. However, the SED-fitted map also has the lowest resolution of the three methods considered here, with final convolved beam size of $25''$, equivalent to $\sim$0.3 pc at the distance of G48. Here we discuss the integrated masses for these three independent methods.

The total mass of G48 can be calculated within a contour of interest using the column density mask (shown in Figure 5):

$$M = \sum_i a_{\rm px}\ m_{\rm H_2}\ N_i({\rm H_2}), \quad (6)$$

where $a_{\rm px}$ is the pixel area, $m_{\rm H_2}$ and $N_i({\rm H_2})$ the column density per pixel.

The masking contours for the IRAC 8 μm extinction map were chosen by visual inspection. This contour results in a threshold of 32.15 MJy sr^{-1}, which corresponds to a column density of 1.34×10^{22} cm^{-2}. A total H_2 mass of 450 $M_\odot$ is enclosed in these contours (see Figure 5, top left panel).

We assume a temperature of 17.3 K (the median point-source temperature; see Section 3.5) for the ATLASGAL-derived column density map (Figure 5, top right panel). The column density threshold is adopted to be at 3$\times$ the rms noise level ($\sim$50 mJy beam^{-1}), corresponding to $N({\rm H_2}) = 0.85 \times 10^{22}$ cm^{-2}. The resulting total mass inside this column density contour is $M({\rm H_2}) = 430\ M_\odot$. For comparison, the median *Herschel*-derived temperature (Figure 5, bottom right panel) in this same region is 19.2 K. If we adopt this temperature instead of 17.3 K, as assumed above, the column density threshold becomes $N({\rm H_2}) = 0.75 \times 10^{22}$ cm^{-2} and the total enclosed ATLASGAL mass is $M({\rm H_2}) = 675\ M_\odot$.

For reference, applying a column density threshold of 1.34×10^{22} cm^{-2} (derived from the IRAC 8 μm column density map) is equivalent to applying an 18 K isotherm to the *Herschel*-derived column density map and results in thresholds that encompass approximately the same spatial extent of the three SCUBA peaks from Ormel et al. (2005). The masses enclosed within these thresholds differ by only 20%–30% compared to the total mass (320 $M_\odot$) of these three peaks.

The total masses for G48 derived from the 8 μm extinction (450 $M_\odot$) and the 870 μm (430 $M_\odot$) emission are remarkably similar. Furthermore, the average column density threshold for both maps corresponds to a *Herschel*-derived total mass of $M({\rm H_2}) = 390\ M_\odot$, also in excellent agreement with the other estimates. Considering the uncertainties in the various assumptions, such as the dust properties, uncertainties in background flux levels, and variations in beam sizes, we find that our mass agreement for G48 is strikingly good across different methods and compared to previous work.

In general, the column density for the diffuse emissions in G48 is comparable for all three methods. For EP, P1, P2, P3, and P4 the peak column densities agree within 18% for the ATLASGAL and the *Herschel* maps. However, the peak column densities derived from the 8 μm extinction are significantly higher than the fitted *Herschel* maps. The peak columns can be higher up to 75%. This might be an effect introduced by the higher spatial resolution of IRAC.

Table 2
Point Sources

Source	R.A. (2000) (hh:mm:ss)	Decl. (2000) (dd:mm:ss)	$F_{24\,\mu m}$ (mJy)	$F_{70\,\mu m}$ (mJy)	$F_{100\,\mu m}$ (mJy)	$F_{160\,\mu m}$ (mJy)	T_L (K)	L_L ($L_\odot$)	M_L ($M_\odot$)	L_H ($L_\odot$)	Comments[a]
1	19:21:49.65	+13:49:31.26	102.7	1764	4086	6931	18.3	48.2	14.3	36.1	S5, P1
2	19:21:50.24	+13:49:39.28	241.1	3702	6931	10712	17.9	35.5	11.9	38.0	S6, P1
3	19:21:50.26	+13:48:18.96	119.5	1730	3659	4745	20.9	17.7	2.4	14.6	S2, P3
4	19:21:47.95	+13:49:20.37	2.8	460	1807	4717	17.2	15.1	6.3	2.8	S15, P2
5	19:21:50.13	+13:47:57.00	27.7	474	902	1474	19.8	5.5	1.0	4.5	S1
6	19:21:40.76	+13:51:17.42	102.7	365	494	693	16.8	2.4	1.2	6.5	
7	19:21:45.58	+13:49:20.51	8.7	299	842	1370	19.5	4.8	1.0	1.7	S12, EP
8	19:21:48.48	+13:49:25.26	-	210	865	4668	17.4	13.3	5.3	-	P2
9	19:21:53.01	+13:48:19.15	34.7	139	174	357	16.5	1.1	0.6	2.8	S3
10	19:21:36.30	+13:52:20.23	31.8	132	780	2209	16.8	7.9	3.8	1.6	S11
11	19:21:35.95	+13:51:59.97	115.5	121	177	521	15.6	1.7	1.3	4.4	S9
12	19:21:40.73	+13:50:54.91	20.2	115	303	894	15.6	3.2	2.4	1.5	S13
13	19:21:31.93	+13:52:51.82	4.6	61	131	516	14.5	1.7	1.9	1.0	

Note. [a] Sx are the associated MIPS 24 μm from van der Wiel & Shipman (2008); Px and EP are the associated submillimeter peaks.

3.5. Point-source Classification

In Table 2 we present the fluxes of the 13 point sources that were detected in all three PACS bands. Except for source 8, all PACS detections have counterparts in MIPS 24 μm. Source 13 was not included in the van der Wiel & Shipman (2008) sample but is detected as a point source at 24 μm (E2 in Figure 3). If one allowed point-source detection in only two PACS bands, this would add only one more obvious point source. This source is also detected at 24 μm (E1) but appears as a diffuse blob of emission at 100 μm, not well matched to the characteristic PSF we expect. However, the projected distance to Source 13 (E2) is $\sim$0.24 pc, which is close to the median separation discussed in Section 4 and therefore would not change the outcome of this discussion. All detected sources are aligned along the mid-infrared filaments of the IRDC. Even though the emission gradient toward the GMC (on the eastern edge of our maps) is brighter and contains some compact emission features, no PACS point sources are detected outside the IRDC filaments.

As in Section 3.3, we used a modified blackbody function to constrain the parameters of these point sources utilizing the dust model by Ossenkopf & Henning (1994, thin ice mantles, 10^5 cm^{-3}). The sources detected at 24 μm cannot be fitted by a single component fit, since the warmer part of the envelope in the direct vicinity of the evolving protostar is contributing significantly to the 24 μm fluxes. Due to the rapidly increasing optical depth toward the innermost regions around the point sources, we only observe surface contributions of surrounding layers of warm dust. The calculations of mass and temperature assume optically thin material.

The 24 μm data are highly sensitive to geometric effects in protostellar cores (see Dunham et al. 2008; Ragan et al. 2012). A protostar in which outflows have carved a cavity in its natal core will be detectable at 24 μm if our line of sight is aligned with the cavity. In particular, the shocked molecular hydrogen, visible as green structures in Figure 1 (right, bottom panel), traces high-velocity outflows. They originate from the rotational S9–S11 transition of excited H_2 in the IRAC 4.5 μm band. They are generally referred to as either "green and fuzzy features" (Chambers et al. 2009) or "extended green objects" (EGOs; Cyganowski et al. 2008). Because the 24 μm flux arises primarily from the warm material immediately surrounding the protostar (and not the cold outer region of the core), we do not include the 24 μm flux in our SED fit to the PACS data but instead fit a second modified blackbody component (see Figure 6). The best fit to the SED results from the sum of these two components. For Source 8, we used one modified blackbody function. The fit parameters are presented in Table 2.

The four most massive sources in our sample are located in the central part of the IRDC in the direct vicinity of the submillimeter peaks P1 and P2. They cover a mass range from 5.4 to 14.3 $M_\odot$. From these sources, Source 8 is the only PACS source without an MIPS 24 μm counterpart. Sources 1 and 2 are the brightest and most massive sources in the sample. They are associated with the SCUBA peak P1 and have a close separation of $\sim$12″. Source 1 appears on top of a compact and diffuse background emission complex. Only a faint source with 0.9 $M_\odot$ is associated with the EP-SCUBA-peak of Ormel et al. (2005). The point sources associated with P3 in the southern part of G48 have only $\sim$1–2 $M_\odot$.

In Figure 7 we present the bolometric luminosities (IRAC to PACS), the envelope masses ($\lesssim$0.15 pc), and the temperatures derived from cold components of the modified blackbody fits. In the luminosity–mass plot the dotted line follows the relation $M_{\rm env} \sim L_{\rm bol}^{0.6}$ and corresponds approximately to a threshold, where 50% of the initial core mass is being converted into stellar mass $M_\star$ (cf. André et al. 2000; Bontemps et al. 1996). Sources with $M_{\rm env} > M_\star$ and a high submillimeter-to-bolometric luminosity ratio $L_{\geqslant 350\,\mu m}/L_{\rm bol} > 0.005$ are considered to be Class 0 (André et al. 2000). Sources 1 and 2, as well as Sources 4 and 8, are detected as single SPIRE sources. But the fitted blackbodies indicate that the submillimeter fluxes should be equal for both sources in each case. For each source we calculate the submillimeter luminosity $L_{\lambda \geqslant 350\,\mu m}$ with 50% of the corresponding SPIRE fluxes. All four sources mentioned before are good Class 0 candidates since $L_{\geqslant 350\,\mu m}/L_{\rm bol} > 0.005$ and $M_{\rm env} > M_\star$. Sources 1 and 2 have the highest envelope masses, and, as indicated by evolutionary tracks (adopted from André et al. 2008), both could evolve into high-mass zero-age main-sequence (ZAMS) stars with $M_{\rm ZAMS} \gtrsim 8\,M_\odot$. These evolutionary tracks assume exponentially declining accretion rates. A recent study by Davies et al. (2011), comparing observations to various accretion models, showed that models with increasing accretion are in best agreement with the observational results. Molinari et al. (2008) used a model with increasing accretion rates to create similar evolutionary tracks. According to these

Table 3
Clumpfinder Parameters

Molecule	Lower Threshold [a] (%)	Step[a] (%)
N_2H^+	5.0	5.0
HCO^+	5.8	5.8
HCN	8.5	3.4
HNC	18.6	9.3
^{13}CO (1–0)	35.2	2.3
^{13}CO (2–1)	31.4	6.3
$C^{18}O$ (2–1)	8.8	5.5

Notes. [a] The minimum detection thresholds and the contrast steps for `clumpfinder` are give in relation to the peak value in the corresponding map.

tracks, Sources 1 and 2 would only evolve into intermediate-mass stars (<8 $M_\odot$). However, it is still unclear on which spatial range a protostar is accreting material. Sources 1 and 2 are associated with the submillimeter peak P1. Due to the resolution of SCUBA compared to PACS, a larger area is traced. Given the light-to-mass ratio for P1 derived by Ormel et al. (2005), still two massive stars ($M_{\rm ZAMS} \gtrsim 8\,M_\odot$) could form in the model from Molinari et al. (2008). Assuming that these sources are in a very young evolutionary stage, they are completely dominated by the accretion luminosity (Krumholz et al. 2007; Hosokawa & Omukai 2009).

3.6. Molecular Line Emission

To determine the parameters from the mapping line data, we used the GILDAS/CLASS[9] package. As mentioned before, we have line detections (CL> 99.73%) associated with the IRDC in the HCO^+, N_2H^+, HCN, HNC, ^{13}CO, and $C^{18}O$ maps. While the line fitting for HCO^+, HNC, and CO is done straightforwardly with a single Gaussian profile, N_2H^+ and HCN have a resolved hyperfine structure with multiple components. For N_2H^+ a model profile containing seven hyperfine-structure components was fitted utilizing the GILDAS/HSF routine. The presented N_2H^+ maps containing the integrated line flux, line width, and velocity correspond to the line center of the strongest component (93.17378 GHz, $J = 1 \rightarrow 0$, $F_1 = 2 \rightarrow 1$, $F = 3 \rightarrow 2$). The hyperfine structure of HCN shows a triplet of components, and in contrast to N_2H^+, the relative line strength of each component varies for different IRDCs (Afonso et al. 1998; Vasyunina et al. 2011). Non-LTE effects especially in the 1–0 lines seem common (see Loughnane et al. 2012). Given the noise level of the HCN map, we could not retrieve an averaged profile. The fitting of the physical parameters is done on the strongest component.

The derived integrated line fluxes, velocities, and line widths are compiled in Table 5. This table gives also the effective radius (see below), the total column density, the abundance, and the traced mass. HCO^+ and HCN are good tracers for dense gas because of their high critical densities. N_2H^+ has a lower critical density (see Table 1) but is not strongly effected by depletion from freeze-outs on grain surfaces. For CO the critical density is, depending on the transition, one or two orders of magnitudes lower than for N_2H^+. The total column density for a certain

[9] http://www.iram.fr/IRAMFR/GILDAS/

Table 4
Upper Limits for Non-detected Line Species for MOPRA

Line	Line Integral Intensity[a] (km s^{-1} K)	Column Density (10^{12} cm^{-1})
CH_3C_2H	0.50	
$H^{13}CN$	0.53	3.8
$H^{13}CO^+$	0.52	0.7
SiO	0.51	1.2
C_2H	0.52	
HNCO	0.48	6.4
HCCCN	0.48	2.0
CH_3CN	0.50	2.9
^{13}CS	0.53	5.9

Notes. [a] Upper limits are the integrated intensity a Gaussian-shaped line with an FWHM of 1 km s^{-1} would have at a peak intensity level of three times the rms noise.

molecular species can be calculated with

$$N_u = \frac{8\pi A_{ul} k \nu^2}{hc^3} \int T_{mb} dv \tag{7}$$

$$N_{\rm tot} = \frac{N_u Q_{\rm rot}(T)}{g_u} \exp(-E_u/T), \tag{8}$$

where A_{ul} is the Einstein coefficient, ν the rest frequency of the transition, N_u and E_u the upper-state column density and energy, $Q_{\rm rot}$ the rotational partition function, and g_u the statistical weight of the upper level. The general physical parameters[10] for the observed lines are given in Table 1. The abundance for a molecule is given in relation to the H_2 column density derived from the SED-fitted map from Section 3.3. The temperature estimates needed to calculate the different molecular abundances were obtained from the same SED fitting. The line emissions from HCO^+, HCN, HNC, and ^{13}CO can be optically thick; therefore, the column densities and abundances provide only lower limits.

For the molecular line maps without any 3σ detection the upper limits for line intensity and column density, based on the noise estimates, are given in Table 4.

Following Ragan et al. (2006), the mass of each clump observed in the line maps is estimated using an assumed distance of 2.6 kpc, an approximate size based on the extent of molecular emission, the molecular column densities, and approximate abundance calculated at the peak of absorption.

In Figure 4 the SPIRE 250 μm images are shown and overplotted by the different line intensity maps (HCO^+, NH_2^+, HCN, HNC, and CO). We used the `clumpfind` (Williams et al. 1994) package to identify the different clumps in the molecular tracers. Four different clumps were found by clumpfinder, hereafter named C1–C4. The detection parameters for `clumpfinder` are given in Table 3. C1, C2, and C3 are detected in HCO^+, HCN, and N_2H^+. An additional clump C4 is detected in HCN. In the ^{13}CO (1–0) GRS map only C1 is detected, while C1 and C2 are detected in the HERA CO (2–1) maps and in HNC. Because `clumpfind` does not make any assumption about the clump morphology, an effective circular radius

$$R_{\rm eff} = \sqrt{A/\pi} \tag{9}$$

[10] The parameters can be obtained from the Leiden Atomic and Molecular Database (LAMBDA). http://www.strw.leidenuniv.nl/~moldata/

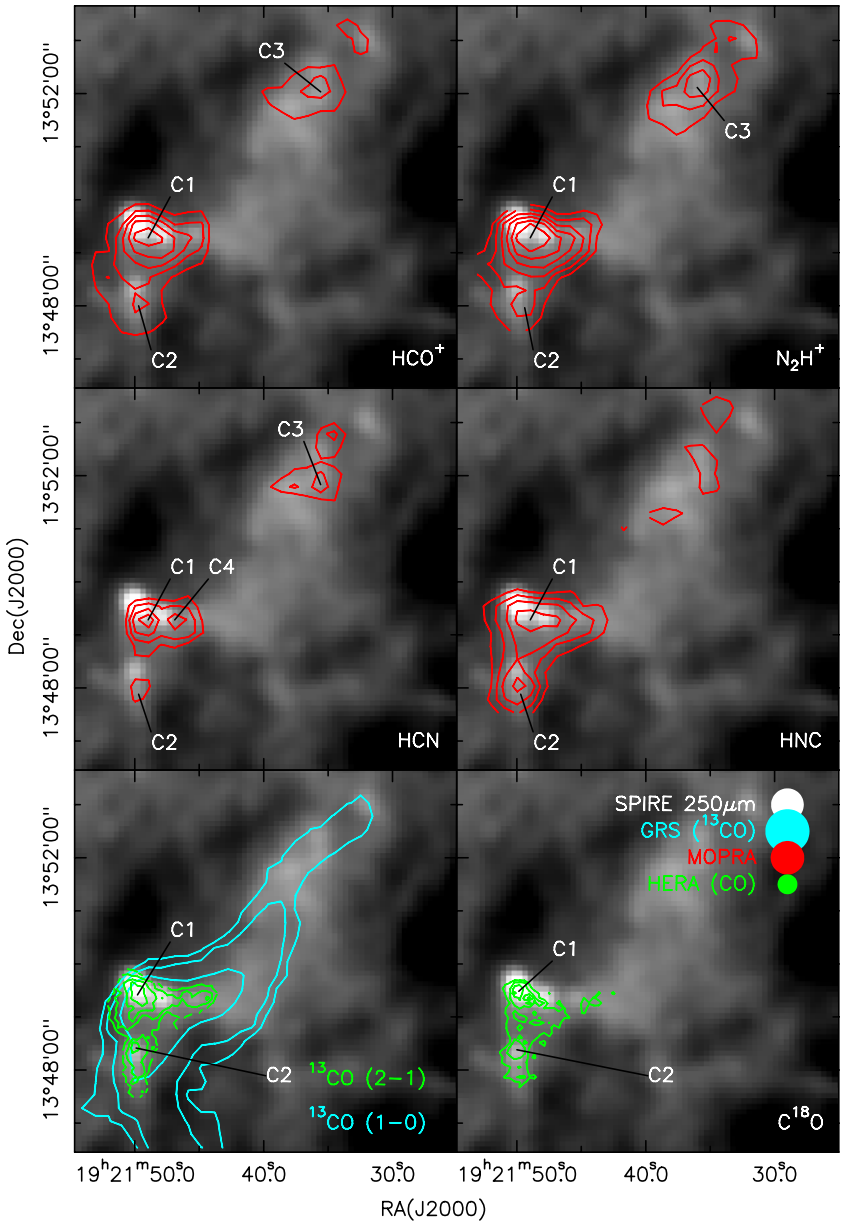

Figure 4. Integrated line intensities of the indicated species are shown as contours overlaying the 250 μm SPIRE map. The contours in the top and middle panels refer to the MOPRA observations, while the bottom panels present the CO data. The beam sizes are indicated in the last panel. The maps are integrated between 32 and 36 km s^{-1}. The contours for the different line transitions are: HCO^+: from 0.3 to 1.5 K km s^{-1} in steps of 0.3 K km s^{-1}; HCN: from 0.2 to 0.8 K km s^{-1} in steps of 0.1 K km s^{-1}; HNC: from 0.2 to 0.8 K km s^{-1} in steps of 0.1 K km s^{-1}; N_2H^+: from 0.5 to 2.0 K km s^{-1} in steps of 0.25 K km s^{-1}; ^{13}CO (1–0): from 0.8 to 2.9 K km s^{-1} in steps of 0.7 K km s^{-1}; ^{13}CO (2–1): from 2.0 to 9.5 K km s^{-1} in steps of 1.5 K km s^{-1}; C^{18}O (2–1): from 0.7 to 2.7 K km s^{-1} in steps of 0.5 K km s^{-1}. (A color version of this figure is available in the online journal.)

is given in Table 5, where A is the area fitted by `clumpfind`. Because the resolution of the HERA observations is three times better than MOPRA, the emission is less diluted and we therefore derive smaller $R_{\rm eff}$. All line maps show the strongest emission in the central part of the IRDC. The maps HCO^+, N_2H^+, HNC, and ^{13}CO show an elongated structure in east-west orientation. HCN shows two distinct peaks (C1, C4); these peaks are shifted by $\sim$30″ southwest of the compact SPIRE emission. All other MOPRA molecular tracers peak at C1, and while the maps appear shifted from the compact SPIRE emission, it is within the pointing error of MOPRA. The peak positions for the HERA CO maps are much better aligned with the SPIRE peaks. In contrast to our observed HCO^+ (1–0) emission, the HCO^+ (3–2) observations from Ormel et al. (2005) show multiple emission peaks. Their eastern emission peak is centered on the SCUBA clump, but the western emission is more diffuse. With the given spatial resolution of MOPRA (38″) it is likely that we only observe a single integrated emission peak for HCO^+ from these multiple unresolved emitting sources.

About 1.′3 southward of the central region another fainter emission peak (C2) can be found for HCO^+, HCN, HNC, N_2H^+, ^{13}CO(2–1), and C^{18}O. It is not coincident with the compact SPIRE and submillimeter emission in this region. In the integrated line flux map for ^{13}CO(1–0), no compact emission clump was found by `clumpfind`. The emission appears just as a diffuse extended lobe from the central peak. In the northwestern part of the IRDC, where only diffuse emission appears in the SPIRE and submillimeter regime, the line data are much more

Table 5
Molecular Line Observations

Source	R.A. (2000) (hh:mm:ss)	Decl. (2000) (dd:mm:ss)	$R_{\rm eff}$[a] (arcsec)	$V_{\rm LSR}$[b] (km s^{-1})	Δv[c] (km s^{-1})	$\int T_{mb} dv$[d] (K km s^{-1})	$N(X)$[e] (10^{12} cm^{-2})	Abundance[f] $\frac{N(X)}{N(H_2)} \times 10^{-10}$	$M(X)$[g] ($M_\odot$)	$M_{\rm vir}$[h] ($M_\odot$)	$\alpha_{\rm vir}$[i]
HCO^+											
C1	19:21:48.958	+13:49:17.04	60	33.90 (0.16)	2.50 (0.11)	3.84	>5.0	>2.0	310	605	1.95
C2	19:21:51.016	+13:47:47.03	50	33.92 (0.12)	2.06 (0.15)	1.64	>2.3	>1.6	100	343	3.43
C3	19:21:35.569	+13:52:02.04	45	34.20 (0.16)	2.99 (0.26)	1.40	>1.6	>1.2	150	649	4.33
HCN											
C1	19:21:48.958	+13:49:17.04	40	34.0 (0.4)	3.6 (0.7)	1.29	>8.9	>3.5	230	837	3.64
C2	19:21:51.016	+13:47:47.03	42	33.8 (0.3)	2.3 (0.5)	0.84	>6.1	>4.3	50	359	7.18
C3	19:21:35.569	+13:52:02.04	40	33.7 (0.4)	2.5 (0.5)	1.04	>7.5	>4.9	115	403	3.50
C4	19:21:46.898	+13:49:17.04	41	34.4 (0.5)	2.6 (0.4)	1.04	>7.2	>3.7	165	448	2.72
HNC											
C1	19:21:48.958	+13:49:17.04	63	33.81 (0.11)	2.50 (0.21)	1.27	>2.7	>1.1	450	636	1.41
C2	19:21:51.016	+13:47:47.03	47	33.77 (0.12)	1.66 (0.18)	2.01	>4.5	>3.1	95	209	2.20
C3	19:21:35.569	+13:52:02.04	39	33.91 (0.28)	2.4 (0.4)	0.83	>1.8	>1.2	140	363	2.59
N_2H^+											
C1	19:21:48.958	+13:49:17.04	72	33.60 (0.17)	1.47 (0.25)	4.69	68.7	27.0	370	251	0.68
C2	19:21:51.016	+13:47:47.03	71	33.59 (0.11)	1.10 (0.22)	2.92	45.0	31.5	85	139	1.64
C3	19:21:35.569	+13:52:02.04	50	33.8 (0.5)	2.9 (0.7)	2.06	31.4	20.5	165	679	4.15
^{13}CO (1–0)											
C1	19:21:48.449	+13:49:17.90	76	33.72 (0.11)	2.11 (0.03)	8.53	$>2.0 \times 10^4$	$>7.9 \times 10^3$	380	546	1.44
^{13}CO (2–1)											
C1	19:21:48.449	+13:49:17.90	19	35.1 (0.22)	2.53 (0.06)	14.9	$>1.6 \times 10^4$	$>6.3 \times 10^3$	60	196	3.27
C2	19:21:51.016	+13:47:47.03	16	34.9 (0.3)	2.49 (0.06)	5.9	$>6.4 \times 10^3$	$>4.5 \times 10^3$	40	160	4.00
$C^{18}O$ (2–1)											
C1	19:21:48.449	+13:49:17.90	18	34.2 (0.3)	1.54 (0.11)	2.3	1.2×10^3	4.9×10^2	55	69	1.25
C2	19:21:51.016	+13:47:47.03	15	34.02 (0.20)	1.88 (0.15)	1.6	8.6×10^2	6.0×10^2	30	86	2.87

Notes. [a] Effective radius from `clumpfinder`; [b] rest-frame velocities; [c] line width; [d] integrated line intensities; [e] column density of the observed molecular species; [f] abundance of the molecular species with respect to H_2, N_{H_2} is calculated from the 870 μm data (and 8 μm extinctions in brackets); [g] mass estimates from molecular line maps, see the text; [h] virial mass $M_{\rm vir} = 126\, R_{\rm eff} \Delta v^2$, see the text; [i] virial parameter $\alpha = M_{\rm vir}/M$.

noisy. For HCO^+, HCN, and N_2H^+ a compact emission peak (C3) can be identified, while ^{13}CO shows an elongated diffuse emission lobe.

The three SCUBA clumps modeled by Ormel et al. (2005) incorporate a mass reservoir of $\sim$320 $M_\odot$. The masses derived for this region from the HCO^+, HCN, HNC, N_2H^+, and ^{13}CO observations differ by up to 20%. Given the uncertainties for the mass estimates, this is a good agreement.

CH_3C_2H is a good temperature probe in dense molecular clouds (e.g., Bergin et al. 1994). We detect four CH_3C_2H transitions: $J = (9\text{–}8)$, $K = 0, 1, 2, 3$ with IRAM single pointing observations positioned on the submillimeter peak P1 (as indicated in the bottom left panel of Figure 5). From the measured integral line intensities we derived the column densities for every particular transition using formulae (1) and (2) from Bergin et al. (1994). Finally, we computed the excitation diagram and estimated the excitation temperature and column density in the region. The resulting temperature is 26 ± 7 K, and the column density is $(3.0 \pm 1.5) \times 10^{12}$ cm^{-2}. All necessary values, like E_u—the upper state energy, g_u—degeneracy, and others, were taken from the CDMS database (Müller et al. 2001).

In Figure 8 (bottom panel) the position–velocity (p–v) plots are shown for ^{13}CO and $C^{18}O$ (2–1). In the $p - v$ plot for $C^{18}O$ only a single velocity component is present. For ^{13}CO two components are present at a 50″ offset, which refers to the spatial position of Source 1 in the PACS points-source catalog and the submillimeter peak P1. Due to the small spread of just $\sim$1.5 km s^{-1}, it is questionable that this structure originates from an outflow cone. Other possible explanations could be a large rotational envelope or just two core-like dense CO structures along the line of sight. With the lack of additional observations with higher sensitivity and spatial resolution, no robust conclusion can be drawn. The line-width maps in Figure 8 are fitted with a single Gaussian. A single Gaussian profile is also fitted there two components are found in the ^{13}CO map (Figure 8, middle plot). The resulting does not differ more than 0.5 km s^{-1} from a fit only on the strongest component.

With typical isotopic abundance ratios of $[^{12}C]/[^{13}C] = 60$ and $[^{16}O]/[^{18}O] = 500$ (Wilson & Rood 1994; Lodders et al. 2009) the HERA ^{13}CO and $C^{18}O$ abundances correspond to $^{12}C^{16}O$ abundances of $\sim$(1–1.5)$\times 10^{-5}$. The expected CO abundance at a given galactocentric distance ($D_{\rm GC}$) can be computed from the following relationship (Fontani et al. 2012, and reference within):

$$X^{\rm E}_{\rm C^{16}O} = 8.5 \times 10^{-5} \exp(1.105\text{–}0.13 D_{\rm GC}/D_{\rm kpc}). \quad (10)$$

For G48 with $D_{\rm GC} = 7.1$ kpc this results in an expected CO abundance of $X^{\rm E}_{\rm C^{16}O} = 1.0 \times 10^{-5}$, thus consequently $X^{\rm E}_{\rm C^{18}O} = 2.0 \times 10^{-7}$ and $X^{\rm E}_{\rm ^{13}CO} = 1.7 \times 10^{-6}$. Comparing these expected values with the observed CO abundances gives the depletion factor

$$f_D = \frac{X^{\rm E}_{\rm CO}}{X^{\rm obs}_{\rm CO}}. \quad (11)$$

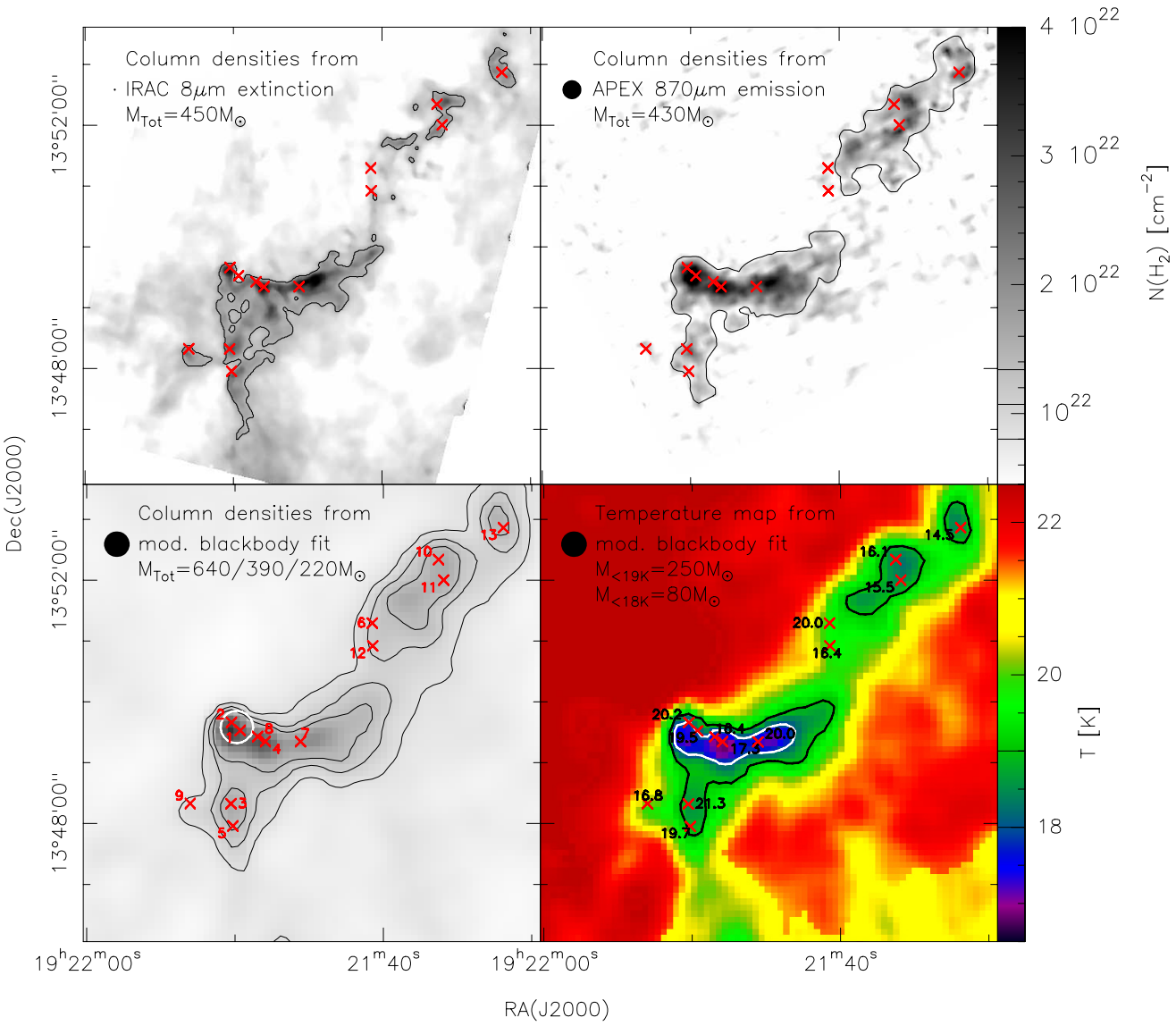

Figure 5. Top two panels show H_2 column density maps obtained from IRAC 8 μm extinction (left) and ATLASGAL 870 μm (right) observations. In these top panels the column density thresholds for the mass determination are shown as contours: within the contour of 1.34×10^{22} cm^{-2} a mass of 450 $M_\odot$ is enclosed for IRAC 8 μm, while the 0.85×10^{22} cm^{-2} ATLASGAL contours contain 430 $M_\odot$ of material. The bottom two panels show the column density (left) and temperature (right) maps from the modified blackbody fitting (Sections 3.3 and 3.4) of the *Herschel*, SCUBA, and ATLASGal maps. The point sources from Section 3.5 are indicated by $\times$. The contours indicate column densities of 0.85×10^{22}, 1.10×10^{22}, and 1.34×10^{22} cm^{-2} and encircle 640, 390, and 220 $M_\odot$, respectively. The white circle indicates the pointing and beam size of the CH_3C_2H observations, which indicates a gas temperature of 26 ± 7 K. The temperatures from the point-source fitting are indicated in the last plot. This temperature map is overplotted with isothermal contours of 19 K (black) and 18 K (white). These isotherms incorporate 250 $M_\odot$ and 80 $M_\odot$ for 19 K and 18 K, respectively.

(A color version of this figure is available in the online journal.)

Using the preceding isotopic abundance ratios results in average depletion factors of $f_D^{^{13}CO} = 3.3$ and $f_D^{C^{18}O} = 3.7$ for G48.

We detected CO_2 ice in the *Spitzer* spectra. In Figure 2 the *Spitzer*/IRS spectrum for Source 2 is shown. The observed shape of the CO_2 ice absorption feature at 15.2 μm is different for the source spectrum compared to the background spectra; the on-source profile is significantly broader and different in shape compared to the nodded background profiles. This implies different ice temperatures and mixing ratios (with, e.g., $H2_O$ and CH_3OH; see White et al. 2009). The low spectral resolution of the IRS/LL2 spectral order does not allow a proper fitting of temperature and mixing ratio to the laboratory data. Most likely the source CO_2 profile originates from ice-coated grains in the dust envelope of the embedded protostar.

The presence of CO_2 ice does not provide direct evidence for CO freeze-out, since the conditions under which the surface conversion $CO + OH \xrightarrow{surf} CO_2 + H$ takes place are still under debate (e.g., Garrod & Pauly 2011). In the gas phase CO_2 is predominantly produced by the following reaction:

$$HCO + O \longrightarrow CO_2 + H$$
$$CO + OH \longrightarrow CO_2 + H$$
$$CO + O \longrightarrow CO_2 + H$$

To the last two reactions an activation energy barrier of 80 K or higher is assigned (Garrod & Pauly 2011). Therefore, gaseous CO_2 creation becomes effective in cores that already have an internal heating source. The CO_2 ice cannot be easily

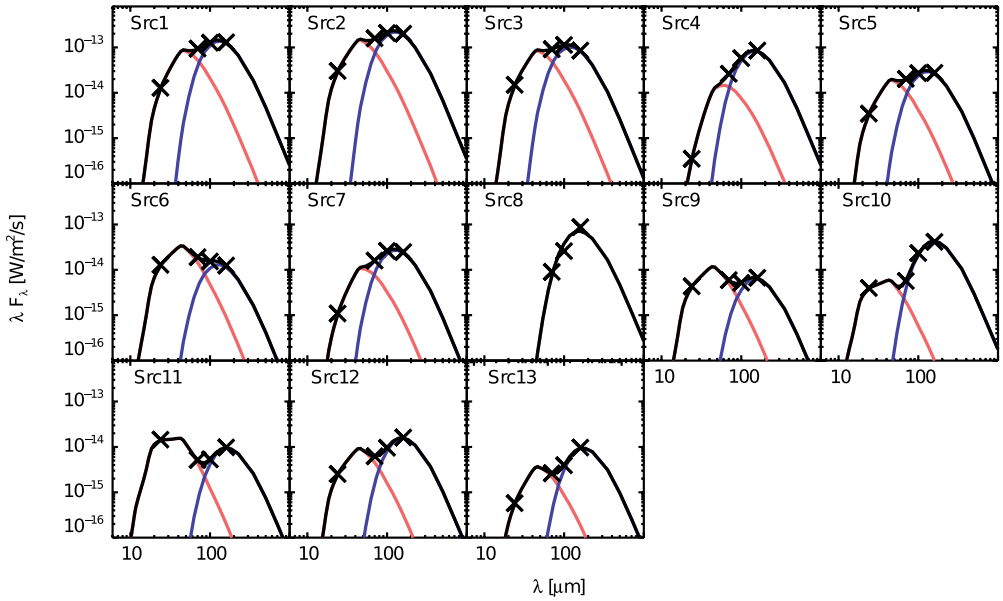

Figure 6. Modified blackbody fits for the detected sources (see Section 3.5).
(A color version of this figure is available in the online journal.)

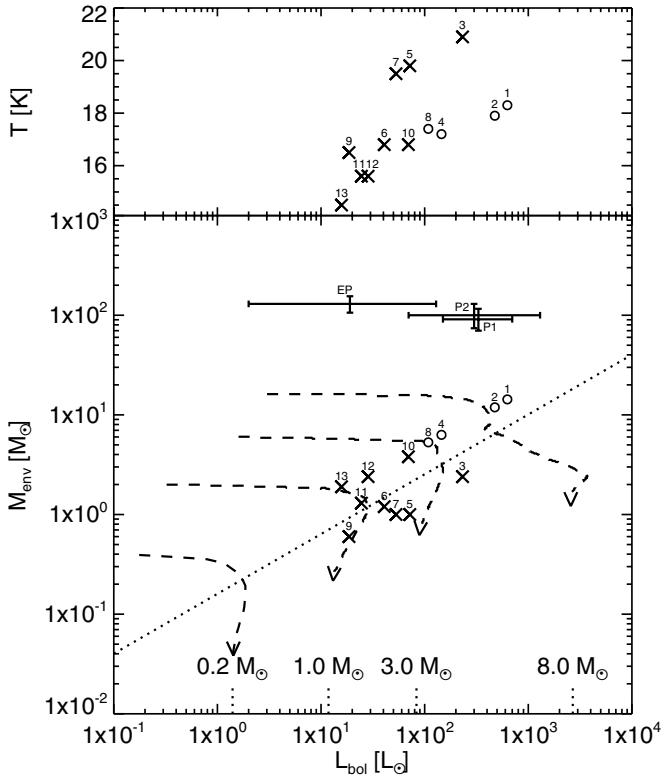

Figure 7. Core temperatures (upper panel) and cold envelope mass (lower panel), derived from the SED fitting of the PACS point sources ($\lesssim$0.15 pc), are plotted against bolometric luminosities. Bolometric luminosities are derived from IRAC, MIPS, and PACS bands. The numbers identify the point sources characterized in Section 3.5. The light-to-mass ratio derived from the submillimeter observation for different peaks (P1, P2, and EP) is plotted as well. In these observations the area of the traced mass reservoir is larger. The dashed lines represent the evolutionary tracks for YSO from André et al. (2008). The final stellar masses (ZAMS) of those tracks are given above the lower axis.

hydrogenated on dust grain surfaces, though, so it will remain a terminal species of the CO evolution in lukewarm regions (D. Semenov 2012, private communication).

4. DISCUSSION

G48 is a quite isolated IRDC at a distance of 2.6 kpc. Consequently, G48 provides nonpareil observations of the collapse and fragmentation of an IRDC without the effects of external feedback, except for the diffuse interstellar radiation field.

We have derived line-of-sight-averaged *Herschel* column density and temperature maps for this source and find a minimum temperature of 16.8 K and outer temperatures of ~23 K. The corresponding column densities range from $\sim 3 \times 10^{22}$ cm^{-2} at the central part of G48 to $\sim 1 \times 10^{22}$ cm^{-2} at the outer edges, where our sensitivity drops sharply.

In this section we will discuss these results in combination with a wealth of other observations with the goal of placing this unique source in an evolutionary context and determining its physical properties.

4.1. Molecular Line Data, CO Freeze-out

The comparison of the line data for G48.66 with other IRDCs shows results for N_2H^+ that are similar to other IRDCs, while the HCO^+ results are different. The average line width of HCO^+ is 2.5 km s^{-1}, which is lower than other IRDCs, with typical values of ~3.2–3.3 km s^{-1} (Vasyunina et al. 2011; Zhang et al. 2011). For N_2H^+ we observed an average line width of 1.8 km s^{-1}. Similar mean line widths were observed for other IRDCs with 1.8 km s^{-1} by Vasyunina et al. (2011) and 2.0 km s^{-1} by Ragan et al. (2006). The mean column density of 2.4×10^{12} cm^{-2} for N_2H^+ in our sample is similar to the column density found for other IRDCs by Gibson et al. (2009). Comparing the amount of CO freeze-out, one finds that the depletion factor is strongly dependent on the chemical age of the IRDC; hence, the depletion varies drastically for different IRDCs. Hernandez et al. (2011) and Hernandez et al. (2012) report a depletion factor of 5 for G035.39−0033, which is a young IRDC of $\gtrsim 7 \times 10^4$ yr similar to G48. In contrast, Miettinen et al. (2011) found no depletion for their sample and argued that this is connected to a more evolved stage of their IRDCs where the increased star formation activity leads to sublimation of CO from the grain surfaces.

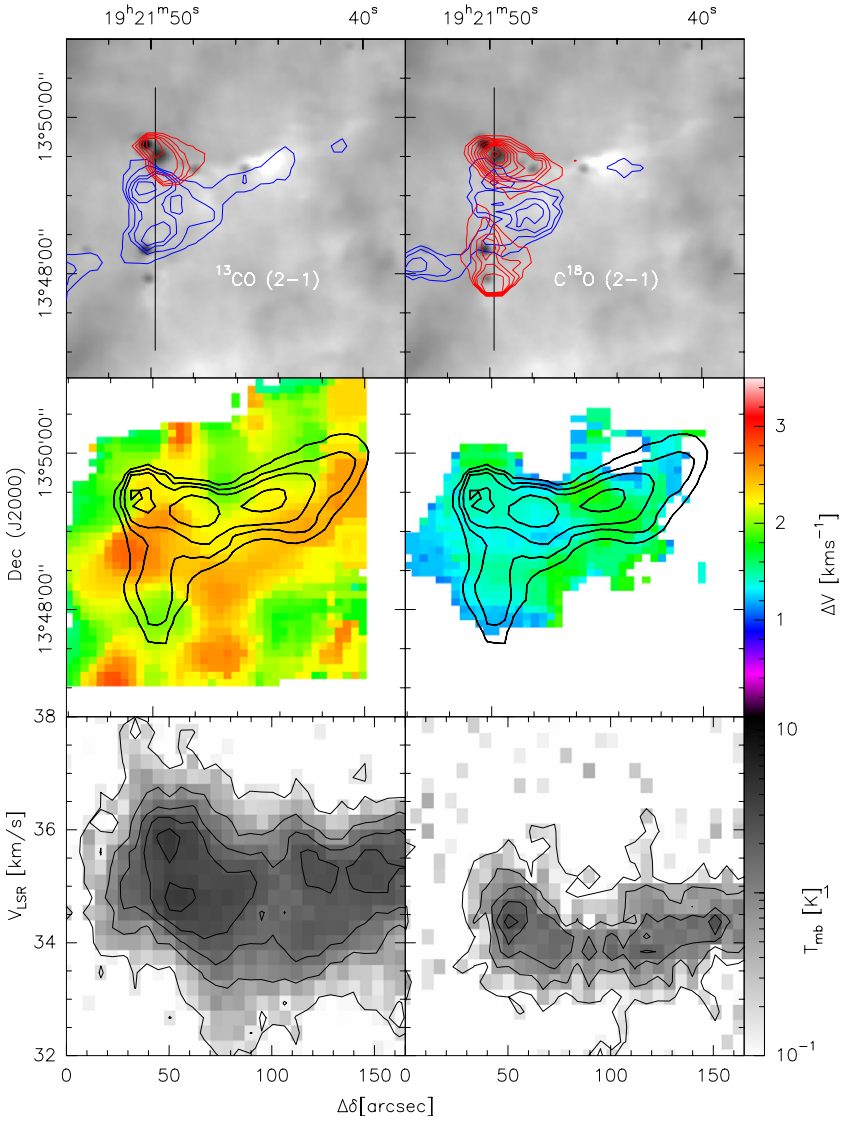

Figure 8. In the top panel the contours of the line intensities for ^{13}CO (left) and C^{18}O (right) are plotted over the inversed PACS 70 μm image. For ^{13}CO (HERA) the blue contour is integrated between 30.0 and 34.0 km s^{-1} and the red contour between 36.0 and 40.0 km s^{-1}. The integration in the C^{18}O HERA map is done over a more narrow range, due to higher noise level, with 32.0–33.5 km s^{-1} (blue) and 34.5–36.0 km s^{-1} (red). The middle plot shows the line width for the HERA CO data. The overplotted contours are the isotherms of 17.5, 18.5, 19.0, and 19.5 K (see Figure 5). The bottom plot shows the position–velocity diagram for ^{13}CO and C^{18}O. The spatial orientation of the p–v plot is indicated in the top panels by a black vertical line.

(A color version of this figure is available in the online journal.)

Fontani et al. (2012) report higher values of f_D = 5–74 for several southern IRDCs; the reason for this higher depletion factors is not completely clear but might be explained by tracing denser regions of the cores by utilizing higher C^{18}O (3–2) transitions, compared to our C^{18}O (2–1) observations. In the gaseous interclump medium N_2H^+ is destructed in the following reaction: $N_2H^+ + CO \longrightarrow HCO^+ + N_2$ (Bergin & Tafalla 2007). The presence of N_2H^+ is consistent with the low CO abundance induced by the freeze-out on the dust-grain surfaces.

By comparing their HCO^+ observations to clump models, Ormel et al. (2005) found an increase of turbulent motions toward the inner part of the clump. Their observations have higher resolution by a factor of two. Therefore, our observations are not good enough to trace down turbulence in the same way, but the increasing MOPRA line widths inward of the clumps are in agreement with the findings of Ormel et al. (2005). Our HERA CO data have a higher resolution than their observations, but due to the low critical density of CO, we trace a larger column that might be dominated by envelope material also along the line of sight. Therefore, CO does not qualify as a good turbulence tracer in dense environments as in our observations.

4.2. Cloud Stability

To assess the dynamical state of the molecular clumps, we calculate the virial mass, using the line width Δv:

$$M_{\rm virial} = k_2 R \Delta v^2, \tag{12}$$

where $k_2 = 126$ for an $n \sim 1/r^2$ profile (MacLaren et al. 1988), R is the effective radius of the molecular clumps, and Δv is the FWHM of the respective line in km s^{-1}. We also calculated the virial parameter α, which is given by the ratio between the kinetic energy $E_{\rm kin}$ and the potential energy $E_{\rm pot}$:

$$\alpha = \frac{2E_{\rm kin}}{E_{\rm pot}} = \frac{M_{\rm vir}}{M}. \tag{13}$$

A value of $\alpha \approx 1$ represents a virial equilibrium, while $1 < \alpha < 2$ is present for pressure-confined clumps (Bertoldi & McKee 1992), $\alpha > 2$ indicates a gravitationally unbound clump, and for $\alpha \ll 1$ the clump is collapsing. The virial mass and the virial parameter are presented in Table 5. We see a large range, from less than 1 to over 7, in virial parameters depending on the species, making it difficult to assess the stability of each clump with certainty. However, while C1 seems to be off equilibrium and just confined by the surface pressure ($\alpha_{C1} = 1.9 \pm 0.7$), C2 and C3 appear to be gravitationally unbound ($\alpha_{C2} = 3.6 \pm 1.3$ and $\alpha_{C3} = 3.6 \pm 0.4$, respectively).

Another crucial parameter is the virial line mass. An isothermal, nonmagnetic, self-gravitating filament in the absence of external pressure is in hydrodynamical equilibrium as long as the mass per unit length does not exceed $m_{\rm vir} = 2\sigma^2/G$, where σ is the velocity dispersion in the gas. If the filament is only thermally supported, the velocity dispersion is given by the thermal sound speed c_s (Ostriker 1964), while in the case of additional turbulence support the velocity dispersion is given by $\sigma = \Delta v/\sqrt{8 \ln 2}$ (Fiege & Pudritz 2000), where Δv is the velocity dispersion. The critical line mass for a thermally supercritical filament in G48 is $M_{\rm line}^{\rm therm} = 24\ M_\odot\ {\rm pc}^{-1}$, whereas the critical line mass calculated by the mean line width of G48, to account also for turbulent motions, is $M_{\rm line}^{\rm crit} = 71\ M_\odot\ {\rm pc}^{-1}$. To highlight the derived line mass, we straightened the filament of G48 utilizing a set of non-uniform cubic splines (Kocsis et al. 1991) and calculated the mass in each pixel. Binning the pixels results in an average line mass of $174\ M_\odot\ {\rm pc}^{-1}$ (see Figure 9). The observed line masses are ~2.5 larger than the critical line mass, indicating that the G48 filament does not contain enough internal support to counter the collapse while the contributions from magnetic fields are expected to be negligible (see below). Line masses observed for other IRDCs seem to exceed $M_{\rm line}^{\rm therm}$. However, for strongly fragmented cores with significantly lower mass in Taurus, line masses similar to $M_{\rm line}^{\rm therm}$, hence predominately thermal support, were observed (Schmalzl et al. 2010). In contrast to G48, several IRDCs show line masses below or similar to $M_{\rm line}^{\rm crit}$. This cannot be explained by the evolutionary stage of the IRDCs alone. The young and starless Coalsack cloud and the adjacent G304.74+01.32 show line masses of less than or equal to $M_{\rm line}^{\rm crit}$ (Beuther et al. 2011; Miettinen 2012, respectively). Also, Hernandez et al. (2012) found the young H filament of G035.39–0.33 to be virial undercritical, although these results rely on several uncertain morphological assumptions about the IRDC. G48 and the Nessie IRDC are more evolved, showing signs of more active star formation such as "green and fuzzy" features, but the latter region still shows line widths a factor of 5 below the critical value for turbulence support (Jackson et al. 2010). Furthermore the presence of magnetic fields does not change the critical line mass significantly (Fiege & Pudritz 2000). However, the higher line mass of $385\ M_\odot$ for the more evolved Orion A cloud (Jackson et al. 2010) supports the view of increasing line masses along the evolutionary sequence.

4.3. Fragmentation and Point-source Separation

In the central part of the IRDC a concentration of point sources is found. The projected median separation of PACS point sources is ~0.3 pc, which is approximately the average separation in the central part of G48. This separation is about three times smaller than in other IRDCs.[11] The median separation in the R1 fragment of the Coalsack dark cloud is even an order of magnitude higher compared to G48 (Beuther et al. 2011), although here this study uses gas/dust peak separations instead of point-source separation. The key question is how to explain these different values. One could assume that we just suffer from a projection effect in G48. Considering that we see an elongated filament and given the observed morphology, it is a feasible assumption that G48 is aligned approximately face-on toward the line of sight. Even if one would assume that G48 is aligned off by $\pi/4$, this would just account for a factor of $\sqrt{2}$. In contrast to G48, the mass reservoir in the IRDCs mentioned above is significantly higher; these other dark clouds do not share the isolated nature of G48. While external feedback and the overall evolutionary stage of the parent cloud might have an important impact on the fragmentation, evaluation of the entire high-mass part of the EPoS sample in Ragan et al. (2012) shows that the average point-source separation is not correlated with the cloud mass (J. Pitann et al., in preparation). Recent molecular line observation of G28.34+0.06 found a separation of just 0.16 pc (Wang et al. 2011) to 0.19 pc (Zhang et al. 2009). The interferometric data analyzed in Wang et al. (2011) show substructures on a ~0.01 pc scale inside the cores.

Given the wide spread of source separation, it should be discussed whether G48 exhibits the same mode of collapse as the IRDCs with larger separation or if some substantially different physical processes can account for the smaller separation. To address this question, we compare the observational results to analytical considerations. A first simple analysis is to compare the source separation to the Jeans length. The separation in G48 is still several times larger than the thermal Jeans length ($\lambda_{\rm J} \approx 0.08$ pc at $10^5\ {\rm cm}^{-3}$, 19 K). Therefore, a thermal Jeans instability is not the dominant fragmentation mode. Fragmentation below this spatial scale has been observed for several massive cores (e.g., Hennemann et al. 2009; Wang et al. 2011).

A way to assess the spatial separation scale is to consider the collapse of a cylinder (with a radius R_c) of an incompressible fluid. It is predicted that several cores form, periodically placed at a characteristic length scale $\lambda_{\rm frag} = R_c$ (Chandrasekhar & Fermi 1953). For an infinite cylinder of isothermal self-gravitating gas the characteristic fragmentation scale is $\lambda_{\rm frag} = 22H$, where H is the isothermal scale height $H = c_s/(4\pi/G\rho_c)^{1/2}$ and c_s the thermal sound speed, G the gravitational constant, and ρ_c the central density in the cylinder (Nagasawa 1987). When an isothermal cylinder with a given radius is embedded into a uniform medium, the separation is $\lambda_{\rm frag} \approx 22H$ for $R \gg H$, but for the opposite case $R \ll H$ the length scale is $\lambda_{\rm frag} \approx 11R$ (Jackson et al. 2010). Given the measured temperatures, the typical thermal sound speed is $c_s = 0.23$ km s^{-1} in G48. With 0.5–0.8 pc the width of the filament is much larger than the scale height. The calculated length scale $\lambda_{\rm frag} = 22H \approx 0.3$ pc (with $n = 10^5\ {\rm cm}^{-3}$, $c_s = 0.23$ km s^{-1}) is the same as the measured separation in G48. However, $\lambda_{\rm frag}$ is affected by uncertainties, since the real value of the central density is unknown. Moreover, the most regular positioning of sources occurs in the central part of the IRDC along a clearly changing temperature profile, which is a distinct derivation from the isothermal assumption.

4.4. Filament Width

The typical filament width seen in Figure 9 is 0.5–0.8 pc. Peretto et al. (2012) and Arzoumanian et al. (2011) find typical filament widths of 0.08–0.1 pc in two different low-mass star-forming regions in the Gould-Belt *Herschel* GTO project.

[11] The separation is about 0.9 pc for the IRDCs G011.11–0.12 (Henning et al. 2010) and G049.40–0.01 (Kang et al. 2011) and 0.75 pc for G304.74–1.32 (Miettinen 2012).

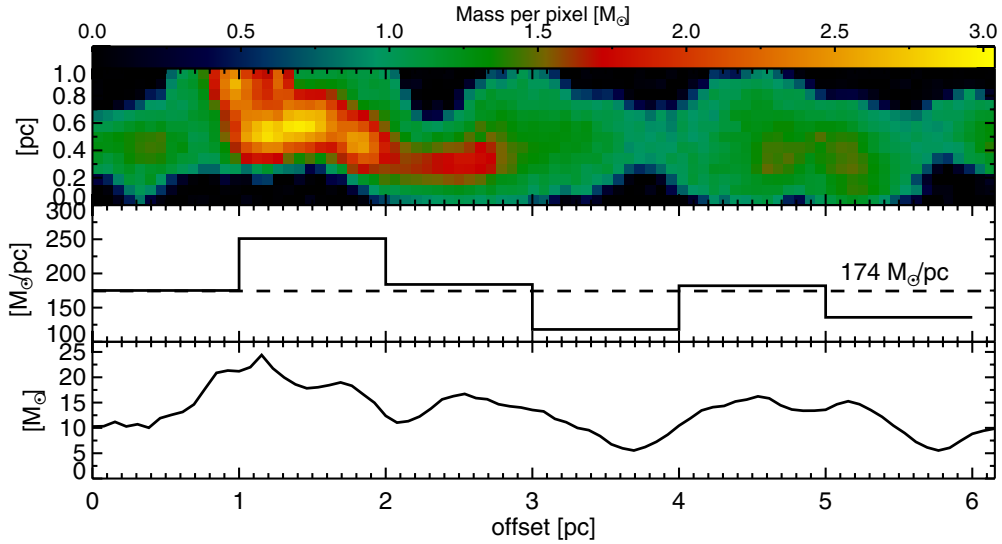

Figure 9. We present the line masses of the straightened filament of G48. The upper panel shows the mass per pixel. The lower plot presents the masses summed over the width of the filament (hence the column of the upper plot). In the middle plot the masses are binned to 1 pc. The average line mass for G48 is given by the dashed line.

(A color version of this figure is available in the online journal.)

These widths are a factor ∼3 smaller compared to the SPIRE 350 μm. IRAC provides a much better resolution, but using the IRAC column density contours shown in Figure 5 results in an estimated filament width of 0.15–0.27 pc. Because these widths are based on the column density threshold, they might be larger than the corresponding FWHM of a fitted Gaussian profile. Arzoumanian et al. (2011) calculated the line mass for their filaments. All filaments have line mass below the average line mass for G48, and most of the filaments are in contrast to G48 below the critical thermal line mass. Also, most of the filaments in the Pipe Nebula are thermally subcritical (Peretto et al. 2012). These results might indicate a trend of larger filament widths toward supercritcal filaments (with respect to turbulence).

4.5. Temperature Profiles

Recent studies have shown that the temperature structure of star-forming regions is non-isothermal. Dust temperature maps for low-mass star-forming Bok globules are shown in, e.g., Stutz et al. (2010, CB 244). Preliminary results for IRDCs were shown by Peretto et al. (2010) for G030.49+0.96 using SED fitting. The minima in their temperature maps are aligned with the column density peaks as in G48 and the subsequent studies. The minimum temperatures for G030.49+0.96 are lower compared to G48 and the two following studies. The work of Battersby et al. (2011) and Beuther et al. (2012) shows similar temperature ranges as for G48. While Battersby et al. (2011) provided a large-scale temperature and column density map, Beuther et al. (2012) present a more detailed study of IRDC 18454 adjacent to the mini-starburst W43. In contrast to IRDC 18454, G48 provides a temperature map of an externally undisturbed filament with the better resolution of the convolution to the SPIRE 350 μm beam (as for G030.49+0.96, IRDC 18454 data were convolved to the SPIRE 500 μm beam). The low temperatures in the cloud centers indicate that they are very young structures.

Wilcock et al. (2012) used a different approach. They compared radiative transfer models of starless purely externally heated cores with the observed embedded cores in IRDCs in the *Spitzer* and *Herschel* bands. They found core temperature profiles with minimum temperatures of 8–11 K, which increase by ∼10–17 K toward the edge of the core. While our temperature mapping only observes an average line-of-sight temperature of the optically thin material, the RT model can retrieve temperature profiles along the line of sight. Since these profiles also probe the optically thick regime, the minimal temperatures are obviously lower. On the other hand, the RT models require an assumption about the geometry of the cores and cannot reassemble the diffuse temperature structure of the whole IRDC.

The temperature profile for G48 shows a drop toward the inner part of the detected submillimeter peaks. Theoretical considerations show that gas-phase coolants, such as C^+ and CO, are efficient for low densities, while the energy transfer between gas and dust is the dominant cooling process for higher densities (e.g., Goldsmith 2001; Glover & Clark 2012). With the presence of IRAC and MIPS 24 μm point sources one would expect to see the imprint of these embedded heating sources in the temperature maps. The SPIRE 350 μm beam size limits the resolution of our temperature maps to ∼0.3 pc so that the embedded heating sources remain unresolved. The dust temperature mapping as presented in this work can provide a versatile tool to test the predicted coupling between gas and dust. Methylacetylene ($CH_3C \equiv CH$) can be used to determine gas temperatures in massive star-forming regions (cf. Miettinen et al. 2006). IRAM pointed observations of CH_3CCH toward the peak position of the submillimeter peak P1 find a gas temperature of 26 ± 7 K. Although this gas temperature is 7 K higher than the dust temperature, the difference is not significant due to the high uncertainty in the gas temperature estimate. However, the trend to higher gas temperatures is a good motivation for further observations of $CH_3C \equiv CH$ or NH_3. Especially gas temperature mapping can provide useful information on the gas–dust coupling at higher densities in molecular clumps. Future work should study the relation between dust temperature structures and gas temperature maps as provided by ammonia (as in Pillai et al. 2006; Ragan et al. 2011) or methylacetylene line observations. Such data should provide further observational evidence for the predicted strong thermal coupling between gas and dust at higher densities.

The northern and southern extents of the IRDC (hosting C2 and C3) show a much flatter temperature profile with higher temperatures compared to the central part of the filament. Furthermore, the column densities are lower toward C2 and C3. This leads to the conclusion that the gas and dust densities are lower in these parts of the G48. Pure isothermal cylindrical collapse can hardly explain this density gradient. Hartmann & Burkert (2007) showed by modeling the density structures for the Orion A cloud that, even in the isothermal case, a simple initial arrangement of a slightly rotating gas sheet can result in filamentary structures with complex density structures.

As in the studies mentioned above, it is a clear finding of this work that the dust temperatures are non-isothermally distributed in an IRDC. What impact could the modeling of thermal profiles have? Thermal line broadening is significantly smaller compared to the observed line widths. Therefore, a change of local temperatures should not have a notable influence on the turbulence structure inside the core. On the other hand, the thermal profile toward the core can play an important role in the support against fragmentation, since the Jeans mass is strongly dependent on temperature as $M_{\rm J} \sim T^{3/2}\rho^{-1/2}$. Theoretical studies of clustered star formation utilizing polytropic equations of states $P \sim \rho^{\gamma}$ and temperature-dependent density profiles $T \sim \rho^{\gamma-1}$ indicate that the number of fragments in a cloud is strongly dependent on the polytropic index γ (Li et al. 2003). For the non-isothermal case ($\gamma \neq 1$) the polytropic index reflects the balance between cooling and heating. Deriving dust temperature maps as in this work is the first step toward a better understanding of spatial distributed cooling and heating inside the core. A more detailed discussion of thermal properties can be found in, e.g., Larson (2005) and Commerçon et al. (2011).

5. SUMMARY

The following gives a brief summary of the results presented in this paper:

1. G48 is a quite isolated, mono-filamentary IRDC. The GMC W51 observed in the same field is twice as distant as G48.
2. The dark filament observed by *Spitzer* does not appear as a large coherent extinction silhouette in the PACS bands. Only the region of highest extinction in the central part is seen in extinction. The filament is clearly seen in emission in the SPIRE bands beyond 250 μm. This is in good agreement with the submillimeter emission maps from SCUBA and ATLASGAL.
3. We present reliable temperature and column density maps based on pixel-by-pixel SED fitting of *Herschel*, ATLASGAL, and SCUBA legacy maps. Regions of low emission outside of the galactic plane were utilized to estimate the global background level for the *Herschel* maps. The locations of the temperature minima are well aligned with the submillimeter and column density peaks. The temperatures drop to 17.5 K in the central part of G48. The heating by embedded MIPS 24 μm point sources is not detected due to beam dilution.
4. We derived a total mass of 390 $M_{\odot}$ for G48 by applying a threshold of 1.1×10^{22} cm^{-2} to the SED-fitted column density maps.
5. "Green and fuzzy" features reveal the central parts of the IRDC as the sites of most active ongoing star formation.
6. We detected 13 point sources in all three PACS bands. Only one source lacks an MIPS 24 μm counterpart.
7. SED fitting to these sources results in core masses of 0.6–14.3 $M_{\odot}$, while the bolometric luminosity ranges between 15 and 630 $L_{\odot}$. The two most massive cores (Sources 1 and 2) have a mass of 14.3 and 11.9 $M_{\odot}$ and a bolometric luminosity of 630 and 475 $L_{\odot}$, respectively. Comparing their light-to-mass ratio to evolutionary models, both sources are likely to evolve into high-mass stars with $M \gtrsim 8\,M_{\odot}$. Applying the definition from low-mass star formation, four cores are good candidates for "Class 0" objects.
8. The average line mass of the G48 filament is 174 $M_{\odot}$ pc^{-1}. Compared to theoretical predictions, the whole filament is collapsing, even under the assumption of internal turbulent support.
9. The point-source separation in G48 is significantly smaller than in other IRDCs, but in good agreement with the predictions by the isothermal cylindrical collapse model.
10. According to our virial analysis, the molecular clumps found in G48 are gravitationally unbound or just pressure confined.
11. Our observations are consistent with previous observations by Ormel et al. (2005), which deduced increasing turbulent motion toward the inner parts of the clumps.
12. We detected several molecular species, such as HCO^+, HCN, HNC, N_2H^+, ^{13}CO, $C^{18}O$ (and CH_3CCH). The mapping observation showed several molecular clumps associated with the submillimeter peaks.
13. We found CO depletion toward the molecular clumps C1 + C2 with a factor of $f_D \approx 3.5$.
14. The low abundance of CO toward the submillimeter peaks P1 and P2 permits relatively high abundances of N_2H^+.

The authors acknowledge the work of the anonymous referee for the valuable comments provided. We thank Zoltan Balog and Marc-Andre Bessel for their help with the optimal reduction of the IRAC/GLIMPSE and MIPSGAL maps. We appreciate the help of Bernhard Sturm with the polynomial background fitting of the *Spitzer*/IRS spectra. We are grateful to Dmitry Semenov for the enlightening discussions regarding astrochemical problems.

This work is based in part on observations made with the *Spitzer Space Telescope*, which is operated by the Jet Propulsion Laboratory, California Institute of Technology, under a contract with NASA. This research made use of Tiny Tim/*Spitzer*, developed by John Krist for the Spitzer Science Center. The Center is managed by the California Institute of Technology under a contract with NASA. This paper is using data from the Mopra radio telescope. The Mopra radio telescope is part of the Australia Telescope National Facility, which is funded by the Commonwealth of Australia for operation as a National Facility managed by CSIRO. This publication makes use of molecular line data from the Boston University-FCRAO Galactic Ring Survey (GRS). The GRS is a joint project of Boston University and Five College Radio Astronomy Observatory, funded by the National Science Foundation under grants AST-9800334, AST-0098562, and AST-0100793. This research has made use of NASA's Astrophysics Data System. This research has made use of the SIMBAD database, operated at CDS, Strasbourg, France. This research made use of APLpy, an open-source plotting package for Python hosted at http://aplpy.github.com. The work of S.R. and A.M.S. was supported by the Deutsche Forschungsgemeinschaft priority program 1573 ("Physics of the Interstellar Medium"). T.V. wishes to thank the National Science

Foundation (US) for its funding of the astrochemistry program at the University of Virginia.

REFERENCES

Afonso, J. M., Yun, J. L., & Clemens, D. P. 1998, AJ, 115, 1111
André, P., Minier, V., Gallais, P., et al. 2008, A&A, 490, L27
André, P., Ward-Thompson, D., & Barsony, M. 2000, Protostars and Planets IV (Tucson, AZ: Univ. Arizona Press), 59
Aniano, G., Draine, B. T., Gordon, K. D., & Sandstrom, K. 2011, PASP, 123, 1218
Arzoumanian, D., André, P., Didelon, P., et al. 2011, A&A, 529, L6
Battersby, C., Bally, J., Ginsburg, A., et al. 2011, A&A, 535, A128
Benjamin, R. A., Churchwell, E., Babler, B. L., et al. 2003, PASP, 115, 953
Bergin, E. A., Goldsmith, P. F., Snell, R. L., & Ungerechts, H. 1994, ApJ, 431, 674
Bergin, E. A., & Tafalla, M. 2007, ARA&A, 45, 339
Bertoldi, F., & McKee, C. F. 1992, ApJ, 395, 140
Beuther, H., Churchwell, E. B., McKee, C. F., & Tan, J. C. 2007, Protostars and Planets V (Tucson, AZ: Univ. Arizona Press), 165
Beuther, H., Kainulainen, J., Henning, T., Plume, R., & Heitsch, F. 2011, A&A, 533, A17
Beuther, H., Tackenberg, J., Linz, H., et al. 2012, A&A, 538, A11
Bontemps, S., Andre, P., Terebey, S., & Cabrit, S. 1996, A&A, 311, 858
Bouwman, J., Lawson, W. A., Dominik, C., et al. 2006, ApJL, 653, L57
Butler, M. J., & Tan, J. C. 2009, ApJ, 696, 484
Butler, M. J., & Tan, J. C. 2012, ApJ, 754, 5
Carey, S. J., Feldman, P. A., Redman, R. O., et al. 2000, ApJL, 543, L157
Carey, S. J., Noriega-Crespo, A., Mizuno, D. R., et al. 2009, PASP, 121, 76
Chambers, E. T., Jackson, J. M., Rathborne, J. M., & Simon, R. 2009, ApJS, 181, 360
Chandrasekhar, S., & Fermi, E. 1953, ApJ, 118, 116
Churchwell, E., Povich, M. S., Allen, D., et al. 2006, ApJ, 649, 759
Commerçon, B., Hennebelle, P., & Henning, T. 2011, ApJL, 742, L9
Cyganowski, C. J., Whitney, B. A., Holden, E., et al. 2008, AJ, 136, 2391
Davies, B., Hoare, M. G., Lumsden, S. L., et al. 2011, MNRAS, 416, 972
Di Francesco, J., Johnstone, D., Kirk, H., MacKenzie, T., & Ledwosinska, E. 2008, ApJS, 175, 277
Diolaiti, E., Bendinelli, O., Bonaccini, D., et al. 2000, A&AS, 147, 335
Dunham, M. M., Crapsi, A., Evans, N. J., II, et al. 2008, ApJS, 179, 249
Egan, M. P., Shipman, R. F., Price, S. D., et al. 1998, ApJL, 494, L199
Fiege, J. D., & Pudritz, R. E. 2000, MNRAS, 311, 85
Fontani, F., Giannetti, A., Beltrán, M. T., et al. 2012, MNRAS, 423, 2342
Garrod, R. T., & Pauly, T. 2011, ApJ, 735, 15
Gibson, D., Plume, R., Bergin, E., Ragan, S., & Evans, N. 2009, ApJ, 705, 123
Glover, S. C. O., & Clark, P. C. 2012, MNRAS, 421, 9
Goldsmith, P. F. 2001, ApJ, 557, 736
Gordon, K. D., Rieke, G. H., Engelbracht, C. W., et al. 2005, PASP, 117, 503
Griffin, M. J., Abergel, A., Abreu, A., et al. 2010, A&A, 518, L3
Hartmann, L., & Burkert, A. 2007, ApJ, 654, 988
Hennemann, M., Birkmann, S. M., Krause, O., et al. 2009, ApJ, 693, 1379
Henning, T., Linz, H., Krause, O., et al. 2010, A&A, 518, L95
Hernandez, A. K., Tan, J. C., Caselli, P., et al. 2011, ApJ, 738, 11
Hernandez, A. K., Tan, J. C., Kainulainen, J., et al. 2012, ApJL, 756, L13
Hosokawa, T., & Omukai, K. 2009, ApJ, 691, 823
Indebetouw, R., Mathis, J. S., Babler, B. L., et al. 2005, ApJ, 619, 931
Jackson, J. M., Finn, S. C., Chambers, E. T., Rathborne, J. M., & Simon, R. 2010, ApJL, 719, L185
Jackson, J. M., Rathborne, J. M., Shah, R. Y., et al. 2006, ApJS, 163, 145
Kang, M., Choi, M., Bieging, J. H., et al. 2011, ApJ, 743, 198
Kauffmann, J., & Pillai, T. 2010, ApJL, 723, L7
Kocsis, E., Trus, B. L., Steer, C. J., Bisher, M. E., & Steven, A. C. 1991, J. Struct. Biol., 107, 6
Krist, J. 2002, TinyTIM/SIRTF User's Guide (Pasadena, CA: SSC)
Krumholz, M. R., Klein, R. I., & McKee, C. F. 2007, ApJ, 656, 959
Kuchar, T. A., & Bania, T. M. 1994, ApJ, 436, 117
Ladd, N., Purcell, C., Wong, T., & Robertson, S. 2005, PASA, 22, 62
Larson, R. B. 2005, MNRAS, 359, 211
Launhardt, R., Stutz, A. M., Schmiedeke, A., et al. 2013, A&A, in press (arXiv:1301.1498)
Li, Y., Klessen, R. S., & Mac Low, M.-M. 2003, ApJ, 592, 975
Lo, N., Cunningham, M. R., Jones, P. A., et al. 2009, MNRAS, 395, 1021
Lodders, K., Palme, H., & Gail, H.-P. 2009, LanB, 4B, 44
Loughnane, R. M., Redman, M. P., Thompson, M. A., et al. 2012, MNRAS, 420, 1367
MacLaren, I., Richardson, K. M., & Wolfendale, A. W. 1988, ApJ, 333, 821
Miettinen, O. 2012, A&A, 540, A104
Miettinen, O., Harju, J., Haikala, L. K., & Pomrén, C. 2006, A&A, 460, 721
Miettinen, O., Hennemann, M., & Linz, H. 2011, A&A, 534, A134
Molinari, S., Pezzuto, S., Cesaroni, R., et al. 2008, A&A, 481, 345
Müller, H. S. P., Thorwirth, S., Roth, D. A., & Winnewisser, G. 2001, A&A, 370, L49
Nagasawa, M. 1987, PThPh, 77, 635
Ormel, C. W., Shipman, R. F., Ossenkopf, V., & Helmich, F. P. 2005, A&A, 439, 613
Ossenkopf, V., & Henning, T. 1994, A&A, 291, 943
Ossenkopf, V., Ormel, C. W., Simon, R., Sun, K., & Stutzki, J. 2011, A&A, 525, A9
Ostriker, J. 1964, ApJ, 140, 1056
Ott, S. 2010, in ASP Conf. Ser. 434, Astronomical Data Analysis Software and Systems XIX, ed. Y. Mizumoto, K.-I. Morita, & M. Ohishi (San Francisco, CA: ASP), 139
Pavlyuchenkov, Y. N., Wiebe, D. S., Akimkin, V. V., Khramtsova, M. S., & Henning, T. 2012, MNRAS, 421, 2430
Perault, M., Omont, A., Simon, G., et al. 1996, A&A, 315, L165
Peretto, N., André, P., Könyves, V., et al. 2012, A&A, 541, A63
Peretto, N., & Fuller, G. A. 2010, ApJ, 723, 555
Peretto, N., Fuller, G. A., Plume, R., et al. 2010, A&A, 518, L98
Pilbratt, G. L., Riedinger, J. R., Passvogel, T., et al. 2010, A&A, 518, L1
Pillai, T., Wyrowski, F., Carey, S. J., & Menten, K. M. 2006, A&A, 450, 569
Pitann, J., Hennemann, M., Birkmann, S., et al. 2011, ApJ, 743, 93
Poglitsch, A., Waelkens, C., Geis, N., et al. 2010, A&A, 518, L2
Ragan, S., Henning, T., Krause, O., et al. 2012, A&A, 547, A49
Ragan, S. E., Bergin, E. A., & Gutermuth, R. A. 2009, ApJ, 698, 324
Ragan, S. E., Bergin, E. A., Plume, R., et al. 2006, ApJS, 166, 567
Ragan, S. E., Bergin, E. A., & Wilner, D. 2011, ApJ, 736, 163
Rathborne, J. M., Jackson, J. M., & Simon, R. 2006, ApJ, 641, 389
Reid, M. J., Menten, K. M., Zheng, X. W., et al. 2009, ApJ, 700, 137
Robitaille, T. P., Whitney, B. A., Indebetouw, R., Wood, K., & Denzmore, P. 2006, ApJS, 167, 256
Roussel, H. 2012, arXiv:1205.2576
Sanhueza, P., Jackson, J. M., Foster, J. B., et al. 2012, ApJ, 756, 60
Sato, M., Reid, M. J., Brunthaler, A., & Menten, K. M. 2010, ApJ, 720, 1055
Schmalzl, M., Kainulainen, J., Quanz, S. P., et al. 2010, ApJ, 725, 1327
Schuller, F., Menten, K. M., Contreras, Y., et al. 2009, A&A, 504, 415
Schuster, K.-F., Boucher, C., Brunswig, W., et al. 2004, A&A, 423, 1171
Shipman, R. F., Frieswijk, W., & Helmich, F. P. 2003, in ASP Conf. Ser. 287, Galactic Star Formation across the Stellar Mass Spectrum, ed. J. M. De Buizer & N. S. van der Bliek (San Francisco, CA: ASP), 252
Simon, R., Jackson, J. M., Rathborne, J. M., & Chambers, E. T. 2006, ApJ, 639, 227
Simon, R., Rathborne, J. M., Shah, R. Y., Jackson, J. M., & Chambers, E. T. 2006, ApJ, 653, 1325
Sodroski, T. J., Odegard, N., Arendt, R. G., et al. 1997, ApJ, 480, 173
Stutz, A., Launhardt, R., Linz, H., et al. 2010, A&A, 518, L87
Stutz, A. M., Rieke, G. H., Bieging, J. H., et al. 2009, ApJ, 707, 137
Swain, M. R., Bouwman, J., Akeson, R. L., Lawler, S., & Beichman, C. A. 2008, ApJ, 674, 482
Urquhart, J. S., Hoare, M. G., Lumsden, S. L., Oudmaijer, R. D., & Moore, T. J. T. 2008, in ASP Conf. Ser. 387, Massive Star Formation: Observations Confront Theory, ed. H. Beuther, H. Linz, & T. Henning (San Francisco, CA: ASP), 381
van der Wiel, M. H. D., & Shipman, R. F. 2008, A&A, 490, 655
Vasyunina, T., Linz, H., Henning, T., et al. 2009, A&A, 499, 149
Vasyunina, T., Linz, H., Henning, T., et al. 2011, A&A, 527, A88
Wang, K., Zhang, Q., Wu, Y., & Zhang, H. 2011, ApJ, 735, 64
Weingartner, J. C., & Draine, B. T. 2001, ApJ, 548, 296
White, D. W., Gerakines, P. A., Cook, A. M., & Whittet, D. C. B. 2009, ApJS, 180, 182
Wilcock, L. A., Ward-Thompson, D., Kirk, J. M., et al. 2012, MNRAS, 422, 1071
Williams, J. P., de Geus, E. J., & Blitz, L. 1994, ApJ, 428, 693
Wilson, T. L., & Rood, R. 1994, ARA&A, 32, 191
Zhang, Q., Wang, Y., Pillai, T., & Rathborne, J. 2009, ApJ, 696, 268
Zhang, S. B., Yang, J., Xu, Y., et al. 2011, ApJS, 193, 10
Zinnecker, H., & Yorke, H. W. 2007, ARA&A, 45, 481